



## Development and Application of Two-Photon Excitation Stimulated Emission Depletion Microscopy for Superresolution Fluorescence Imaging in Thick Tissue

The Harvard community has made this article openly available. [Please share](#) how this access benefits you. Your story matters.

Citation	No citation.
Accessed	February 19, 2015 12:26:13 PM EST
Citable Link	<a href="http://nrs.harvard.edu/urn-3:HUL.InstRepos:11051181">http://nrs.harvard.edu/urn-3:HUL.InstRepos:11051181</a>
Terms of Use	This article was downloaded from Harvard University's DASH repository, and is made available under the terms and conditions applicable to Other Posted Material, as set forth at <a href="http://nrs.harvard.edu/urn-3:HUL.InstRepos:dash.current.terms-of-use#LAA">http://nrs.harvard.edu/urn-3:HUL.InstRepos:dash.current.terms-of-use#LAA</a>

*(Article begins on next page)*

HARVARD UNIVERSITY  
Graduate School of Arts and Sciences



DISSERTATION ACCEPTANCE CERTIFICATE

The undersigned, appointed by the  
Committee on Higher Degrees in Biophysics  
have examined a dissertation entitled

**Development and Application of Two-photon Excitation  
Stimulated Emission Depletion Microscopy for Superresolution  
Fluorescence Imaging in Thick Tissue**

presented by **Kevin T. Takasaki**

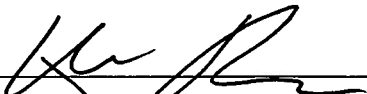
candidate for the degree of Doctor of Philosophy and hereby  
certify that it is worthy of acceptance.

Signature  \_\_\_\_\_

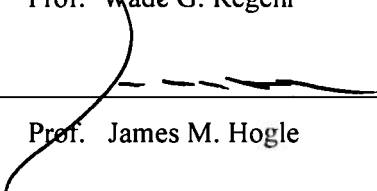
Typed name: Prof. David A. Boas

Signature  \_\_\_\_\_

Typed name: Prof. Adam E. Cohen

Signature  \_\_\_\_\_

Typed name: Prof. Wade G. Regehr

Signature  \_\_\_\_\_

Typed name: Prof. James M. Hogle

Date: May 2, 2013



*Development and Application of Two-photon Excitation Stimulated Emission Depletion  
Microscopy for Superresolution Fluorescence Imaging in Thick Tissue*

A dissertation presented

by

Kevin T. Takasaki

to

The Committee on Higher Degrees in Biophysics

in partial fulfillment of the requirements

for the degree of

Doctor of Philosophy

in the subject of

Biophysics

Harvard University

Cambridge, Massachusetts

May 2013

© 2013 Kevin T. Takasaki  
All rights reserved.

Development and Application of Two-photon Excitation Stimulated Emission Depletion  
Microscopy for Superresolution Fluorescence Imaging in Thick Tissue

**Abstract**

Two-photon laser scanning microscopy (2PLSM) allows fluorescence imaging in thick biological samples where absorption and scattering typically degrade resolution and signal collection of 1-photon imaging approaches. The spatial resolution of conventional 2PLSM is limited by diffraction, and the near-infrared wavelengths used for excitation in 2PLSM preclude the accurate imaging of many small subcellular features of neurons.

Stimulated emission depletion (STED) microscopy is a superresolution imaging modality which overcomes the resolution limit imposed by diffraction and allows fluorescence imaging of nanoscale features. In this thesis, I describe the development of 2PLSM combined with STED microscopy for superresolution fluorescence imaging of neurons embedded in thick tissue. Furthermore, I describe the application of this method to studying the biophysics connecting synaptic structure and function in dendritic spines.

## Table of Contents

1.	Introduction.....	1
1.1.	Motivation .....	1
1.2.	Fluorescence microscopy in neurobiology.....	1
1.3.	Superresolution fluorescence microscopy.....	3
1.4.	Description of thesis.....	3
2.	Concepts and theory.....	4
2.1.	Fluorescence microscopy .....	4
2.1.1.	Flourescence .....	4
2.1.2.	Two-photon excitation laser-scanning microscopy .....	5
2.1.3.	Resolution limit of conventional fluorescence microscopy.....	6
2.1.4.	Resolution enhancement by deconvolution .....	7
2.1.5.	Linear deconvolution .....	8
2.2.	Stimulated emission depletion microscopy.....	10
2.2.1.	Stimulated emission.....	10
2.2.2.	Stimulated emission depletion .....	11
2.2.3.	Resolution enhancement in STED microscopy .....	12
2.2.4.	Theory of STED ring formation .....	13
3.	Two-photon excitation STED microscopy with continuous wave (CW) STED .....	18
3.1.	Introduction .....	18
3.2.	Design and operation of the CW STED2P microscope .....	18
3.2.1.	Description of the microscope .....	18
3.2.2.	Co-alignment of excitation and STED lasers.....	21
3.2.3.	Two-photon excitation and CW STED of fluorescent dyes .....	21
3.2.4.	CW STED2P imaging of fluorescent beads.....	23
3.3.	CW STED2P imaging in brain tissue.....	26
3.3.1.	Consideration of refractive index mismatch.....	26
3.3.2.	Sample preparation, materials, and methods .....	27
3.3.3.	Enhanced resolution of dendritic spines .....	28
3.3.4.	Effect of lateral resolution enhancement on 3D reconstruction.....	31
3.3.5.	Use of CW STED2P for morphological analysis .....	33
3.3.6.	Consideration of phototoxicity of STED imaging in tissue.....	35
3.4.	Discussion .....	37
4.	Two-photon excitation STED microscopy with pulsed STED.....	39
4.1.	Introduction .....	39
4.2.	Design and operation of the pSTED2P microscope.....	40
4.2.1.	Description of the microscope .....	40
4.2.2.	Co-alignment of excitation and STED laser pulses .....	44
4.2.3.	Demonstration and characterization of pulsed STED.....	44
4.2.4.	Interaction of excitation and STED laser polarization.....	46
4.2.5.	pSTED2P imaging of 40 nm fluorescent beads.....	48
4.3.	pSTED2P imaging in brain tissue .....	50
4.3.1.	Sample preparation, materials, and methods .....	50
4.3.2.	Comparison of CW and pulsed STED resolution.....	51
4.3.3.	Effect of depth on the resolution of STED imaging in tissue.....	52

4.3.4.	Effect of depth on the efficiency of STED .....	54
4.3.5.	Imaging of dendritic spines with 60 nm resolution .....	57
4.3.6.	Accurate imaging and measurement of dendritic spine morphology .....	59
4.4.	Discussion .....	62
5.	Application of pSTED2P to studying the biophysics of dendritic spines.....	64
5.1.	Introduction .....	64
5.2.	Dendritic spines as biochemical compartments .....	64
5.2.1.	Diffusive compartmentalization in dendritic spines .....	64
5.2.2.	Morphological determinants of diffusional transfer in dendritic spines .....	66
5.3.	Dendritic spines as electrical compartments .....	69
5.3.1.	Electrical compartmentalization in dendritic spines .....	69
5.3.2.	Morphological determinants of electrical compartmentalization of spines .....	70
5.4.	Discussion .....	73
6.	Summary and future directions.....	74
6.1.	Thesis summary.....	74
6.2.	Future directions.....	74
6.2.1.	Improving depth penetration of two-photon excitation STED microscopy .....	74
6.2.2.	Identification and implementation of alternative fluorophores .....	75
6.2.3.	Biophysical, structural, and functional studies of nanoscale systems .....	76



## **Acknowledgements**

This dissertation would not have existed without the support of many people, of whom only an incomplete list could be rendered here. I can only be grateful and humbled by the recognition of having received so much, and so much more than deserved.

It is a privilege to be able to thank my advisor, Professor Bernardo Sabatini, for providing the inspiration and support that made this research possible, as well as for invaluable years of guidance and mentoring. It is likewise a privilege to thank my coworkers and friends in the Sabatini lab for years of friendship, collaboration, and the benefit of a supportive community of excellent people and impressive scientists. I would especially like to thank Professor Jun Ding for his essential contributions to the research in this thesis, as well as to my personal experience as a student in the lab and to my training as a scientist.

I would like to thank the faculty who have personally mentored and supported me in my graduate training: Professors Wade Regehr, Gary Yellen, Bruce Bean, Adam Cohen, and David Boas. I would also like to thank Professor Jim Hogle and Michele Jakoulov for making the unique experience and training possible for myself and countless others who have been so fortunate as to be students in the Biophysics program.

I would of course like to thank my family for their love, and for raising and supporting me for all of these years, through the thick and the thin of life. Lastly, I would like to thank my wife, whose love and support I could not have done without, and with whom everything is shared, the joy and hardship, the struggle and the victory.

*I have been thinking how very gently I have been always dealt with. I have never had a violent shove in all my life. The only desire I can have is like David to serve my own generation by the will of God, and then fall asleep.*

- *James Clerk Maxwell*

## **1. Introduction**

### **1.1.Motivation**

The history of neuroscience demonstrates that much neurobiology can be accomplished by improving microscopy. Over 100 years ago, staining techniques allowing the visualization of individual cells by light microscopy enabled the first characterization of the fine organization of neural tissue and the identification of the brain's cellular components in the pioneering work of Camillo Golgi, Santiago Ramon y Cajal, and their contemporaries, which established foundations of modern neurobiology. Over 50 years ago, the invention of the electron microscope and its application to studying the brain led to unprecedented insight into the molecular composition and nanoscale complexity of the synapse. And in the past 20 years, the development and adoption of green fluorescent protein (GFP) and its derivatives as tools for cell labeling and protein tagging have had a profound and far-reaching impact on many fields of research, including neurobiology.

### **1.2.Fluorescence microscopy in neurobiology**

In modern times, fluorescence microscopy has become widely used in neurobiology to reveal the structure and function of the brain on a broad range of spatial and temporal scales. Fluorescence imaging provides unique access to the biology of the brain due to its spatiotemporal resolution that can keep up with dynamic processes on the millisecond timescale with sub-micron accuracy, its relative non-destructiveness to biological samples, its ability to identify cells and cellular components labeled with genetically encoded fluorescent markers, and its compatibility with other powerful experimental techniques, such as electrophysiology and optogenetics.

Even more recently, the development of multiphoton fluorescence microscopy (Denk et al., 1990) for imaging in live tissue has continued to revolutionize and extend the usefulness of fluorescence imaging, as the 3-dimensional architecture and complex circuitry of the brain often requires performing experiments in thick or intact tissue. Conventional widefield and confocal fluorescence techniques are not well suited to imaging within brain tissue where scattering, absorption, and out-of-focus fluorescence strongly degrade image quality and lead to photobleaching and toxicity. The development of two-photon laser scanning microscopy (2PLSM) has enabled the use of tissue-penetrating, near-infrared wavelengths that produce nonlinear excitation restricted to the focal plane. The application of 2PLSM to neurobiology has allowed unprecedented high-resolution fluorescence imaging within scattering tissue and has been used, for example, to visualize the morphological plasticity of dendritic spines in living animals, to study the properties of individual synapses in brain slices, and to examine microscale biochemical signaling within neurons.

Despite the advantages of fluorescence imaging and 2PLSM, many biologically important features of neurons are not resolvable by confocal microscopy and 2PLSM because of the physical limit on resolution of fluorescence microscopy resulting from the wave propagation of light, commonly known as the diffraction limit. These unresolvable features include synaptic structures, such as filopodia and small dendritic spines, the morphologies of dendritic spine necks, the structure of the post-synaptic density, the organization of the presynaptic terminal, and perhaps additional structures that have yet to be seen or described.

### **1.3. Superresolution fluorescence microscopy**

Several far-field fluorescence imaging methods have recently been described that allow superresolution imaging, defined as imaging capable of overcoming limitations on resolution imposed by the wave propagation of light. Saturated structured illumination microscopy (SSIM) (Gustafsson, 2005), stochastic optical reconstruction microscopy (STORM) (Rust et al., 2006), photoactivated localization microscopy (PALM) (Betzig et al., 2006), and stimulated emission depletion (STED) microscopy (Klar et al., 2000) are well known examples of such superresolution methods.

### **1.4. Description of thesis**

This thesis describes the development of combined STED and two-photon excitation microscopy for superresolution fluorescence imaging of neurons embedded in thick slices of live tissue and the application of superresolution fluorescence imaging to biophysical studies of the correspondence between the structure and function of dendritic spines.

In chapter 2, I will introduce and summarize essential concepts and relevant theory concerning 2PLSM and STED. In chapter 3, I will describe the development and demonstration of resolution enhancement in tissue by STED2P implemented with a continuous wave STED laser. In chapter 4, I will describe the development and demonstration of superresolution imaging with 60 nm resolution by STED2P implemented with a pulsed STED laser. In chapter 5, I will describe the application of pulsed STED2P for studying the biophysics of dendritic spines. In Chapter 6, I will provide a summary of the thesis and discuss future research directions.

## 2. Concepts and theory

### 2.1. Fluorescence microscopy

#### 2.1.1. Fluorescence

Fluorescence describes light emission resulting from the spontaneous transfer of energy from the electronic state of atoms, molecules, or other material systems, into energy of the electromagnetic field (i.e. photons). The rate,  $k_{em,\alpha}$ , at which a two-level system coupled to the electromagnetic field by the electric dipole interaction transitions from its excited state to the ground state by emitting into a mode  $\alpha$  of the electromagnetic field can be expressed as

$$k_{em,\alpha} \propto \bar{n}_\alpha + 1 \quad (2.1)$$

where  $\bar{n}_\alpha$  is the average number of photons already present in the mode.  $k_{em,\alpha}$  is then a sum of two emission processes. The first, which is proportional to the average incident photon number,  $\bar{n}_\alpha$ , describes emission that is enhanced by interaction with photons present in the mode. This first process is known as stimulated emission. The second, which is a constant independent of  $\bar{n}_\alpha$ , describes the rate of emission that occurs in the absence of any stimulating fields. This second process is known as spontaneous emission, or fluorescence.

For fluorescent molecules (fluorophores) in aqueous solution, vibrational and rotational modes form energy sublevels within the electronic excited and ground states. According to the Franck-Condon principle, electronic transitions involving the absorption and emission of light generally populate higher energy vibrational sublevels which, at physiological temperature ( $\sim 300$  K), equilibrate on timescales of tens of picoseconds, undergoing rapid relaxation to lower energy sublevels through interaction with the

environment. Because the fluorescence lifetimes of many fluorophores are long (~1 ns) compared to this relaxation time, fluorescence generally occurs after relaxation and energy loss, which results in a Stokes shift, or a red-shift of the spontaneous emission spectrum of a fluorophore relative to its absorption spectrum.

### **2.1.2. Two-photon excitation laser-scanning microscopy**

Fluorescence microscopy techniques detect fluorescence emission to measure the spatial distribution of emitters in a sample, thereby producing an image. In laser-scanning microscopy, a focused laser beam is scanned through the sample, producing excitation of fluorophores that interact with the laser field. Fluorescence emission is then collected by a condenser or objective lens and relayed to the photodetector, usually a photomultiplier tube (PMT) or semiconductor photodiode (PD).

Generally, the advantages of laser-scanning microscopy over widefield techniques are conferred by the confinement of excitation to the light cone formed by the focused laser, as opposed to full sample illumination in the case of many widefield systems. In the case of confocal microscopy, the lateral confinement of excitation at the focus is supplemented by a pinhole placed in an image plane conjugate to the focal plane. This pinhole rejects background fluorescence produced by out-of-focus excitation, thus conferring optical sectioning, that is axial, or z-axis, resolution. Due to its high resolution in 3 dimensions, confocal microscopy has become a widely used, fluorescence imaging technique in biology.

Special considerations arise in the use of fluorescence microscopy for imaging in thick samples of living tissue. Absorption and scattering of optical wavelengths in tissue hinder penetration of the excitation light and collection of fluorescence. One-photon

excitation techniques suffer from increased background fluorescence due to out-of-focus and scattered excitation light which degrades resolution and reduces signal-to-noise, as well as produces photobleaching and associated toxicity throughout the sample. Two-photon excitation permits the use of longer, near-infrared, excitation wavelengths which experience less absorption and scattering in tissue. In addition, the nonlinearity of excitation produced by the simultaneous absorption of two photons reduces background fluorescence and photobleaching, as excitation is confined to a femtoliter volume in the focal plane and is dominated by the ballistic (unscattered) component of the excitation light. Because two-photon excitation affords intrinsic 3-dimensional sectioning, a confocal pinhole is not required for axial resolution and all fluorescence can be collected, thus reducing signal degradation due to scattering of the emitted fluorescence. Because of these advantages, two-photon laser-scanning microscopy (2PLSM) permits fluorescence imaging from several hundreds of microns to up to 1 millimeter deep in thick tissue of acute slices or the intact brain.

### **2.1.3. Resolution limit of conventional fluorescence microscopy**

Image formation in laser-scanning fluorescence microscopy can be idealized as a convolution of the sample emitter distribution,  $S(\vec{\rho}')$ , and the distribution of light intensity or excitation probability around the laser focus,  $Ex(\vec{\rho}')$ , so that the image,  $Im(\vec{\rho})$ , is given by,

$$Im(\vec{\rho}) = S(\vec{\rho}') \otimes Ex(\vec{\rho}') \quad (2.2)$$

If the sample distribution is a point, or a delta function mathematically, then the image formed is of the excitation volume,  $Ex(\vec{\rho}')$ , itself, and is also called the point-spread-function (PSF). In Fourier space, the convolution operation in (2.2) becomes a product of



the Fourier transform of the sample distribution and the Fourier transform of the PSF, also known as the optical transfer function (OTF). Blurring due to the non-zero width of the PSF equates to filtering of the spatial frequencies of the sample distribution due to the finite bandwidth of the OTF, and the reciprocal of the cutoff frequency of the OTF can be used to define the resolution of an imaging system. The cutoff frequency resulting from the diffraction of light through a finite aperture, described by Ernst Abbe in 1873 (Abbe, 1873), imposes a limit on spatial resolution in the far-field, or equivalently the width of the PSF,  $\Delta r$ , determined by the wavelength,  $\lambda$ , and numerical aperture,  $NA$ , of the microscope as,

$$\Delta r \sim \frac{\lambda}{2NA}. \quad (2.3)$$

With regard to conventional laser-scanning fluorescence microscopes, the consequence of the Abbe limit is that the minimal size of the excitation volume, or PSF, is determined by the wavelength of the excitation light and the NA of the microscope objective. Thus, structures with dimensions smaller than the width of the PSF, or about half the wavelength of the excitation light, are subject to significant filtering which leads to blurring and distortion. For conventional fluorescence microscopes, the Abbe limit prescribes a maximal resolution in the range of several hundreds of nanometers, of which 2PLSM resolution is generally limited to ~300-400 nm due to its use of long excitation wavelengths.

#### **2.1.4. Resolution enhancement by deconvolution**

The operation in (2.2) mathematically describes the process by which the distribution of fluorophores in the sample, represented by  $S(\vec{\rho}')$ , forms a fluorescence image,  $Im(\vec{\rho})$ , as a linear convolution with  $Ex(\vec{\rho}')$ . The concept of computationally deriving  $S(\vec{\rho}')$  from

$Im(\bar{\rho})$  by “undoing” (2.2), or “deconvolving” the image to obtain the sample distribution, motivates a large class of algorithms and methods within the space of computational approaches to image enhancement. A detailed discussion of the body of research concerning image recovery is beyond the scope of this thesis, but consideration of the example of linear deconvolution will highlight several challenges that hinder the application and usefulness of computational image recovery methods in general. Many of these difficulties result from the inverse problem of image recovery being “ill-posed.” A more thorough discussion of the use and limits of image recovery may be found in the literature. (Bertero and Boccacci, 1998)

### 2.1.5. Linear deconvolution

In Fourier space, (2.2) becomes a multiplication operation. That is,

$$Im = \tilde{S} \cdot Ex \tag{2.4}$$

where quantities with a tilde represent the Fourier transform of the function under the tilde. Representation in Fourier space shows that the convolution in (2.2) is equivalent to linear filtering in (2.4). Linear deconvolution methods attempt to recover  $S(\bar{\rho}')$  by “unfiltering”  $Im(\bar{\rho})$  in Fourier space. This can be achieved by multiplying the Fourier transform of  $Im(\bar{\rho})$  by an “inverse filter,” usually the reciprocal of the OTF, or  $Ex^{-1}$ , which reverses, or equalizes, the filtering. In this approach, a problem arises if the OTF is non-zero within only a finite range of frequencies. The OTF being zero outside of this range causes the inverse filter to blow up at these frequencies, generally forcing the exclusion of these frequencies from analysis and methodically introducing loss of information. The problem of a finite OTF and inverse filter blow-up is an example of the inverse problem being ill-posed. In this case, the ill-posed-ness results from the OTF

being bandlimited. Bandlimiting of the OTF allows many possible sample distributions for  $S(\vec{\rho}')$  to satisfy (2.2) and produce the observed  $Im(\vec{\rho})$ , and thus, a unique solution for  $S(\vec{\rho}')$  cannot be derived from  $Im(\vec{\rho})$ . The lack of a unique solution raises fundamental questions, namely, “How does one identify the ‘best’ solution?” and subsequently, after estimating  $S(\vec{\rho}')$  from the range of possibilities, “Under what conditions and for what purposes is the estimate justified or sufficiently accurate?” These questions frequently arise in computational approaches to image recovery and are difficult to address in general.

The problem of ill-posed-ness is further amplified when one acknowledges that  $Im(\vec{\rho})$  cannot be determined exactly, or measured with infinite accuracy, in a real experiment. Sources of uncertainty or noise in determining  $Im(\vec{\rho})$  can result from both systemic error and natural variability. Limiting or accounting for all of these sources of uncertainty may be experimentally impossible, and the presence of uncertainty limits the use of image recovery techniques due to noise amplification and artifact production. In the case of linear deconvolution, multiplication with the inverse filter problem can amplify noise and increase the contribution of noise in the recovered  $S(\vec{\rho}')$  to the point where the contribution of the sample cannot be discriminated (Mertz, 2010). Again, the questions posed at the end of the previous paragraph must be addressed with difficulty.

In contrast, in optical superresolution the problem of (2.2) is solved in the forward direction. The filtering produced by the OTF, or equivalently the size of the PSF, is physically reduced, so that the measured  $Im(\vec{\rho})$  more closely resembles  $S(\vec{\rho}')$  and no computational enhancement is necessary. Issues associated with mathematically solving

inverse problems under experimental conditions are then avoided. One method by which the PSF can be physically reduced will now be discussed in the following section.

## 2.2. Stimulated emission depletion microscopy

### 2.2.1. Stimulated emission

As was seen from (2.1), the presence of photons interacting with a system in an excited state can generate stimulated emission at a rate proportional to the average photon number, or intensity, of the incident light. The constant of proportionality can be calculated from the stimulated emission cross-section which describes the probability of stimulated emission per incident photon per molecule into the given mode of the field. Stimulated emission returns the system to the ground state from which fluorescence can no longer occur (Figure 2.1 a).

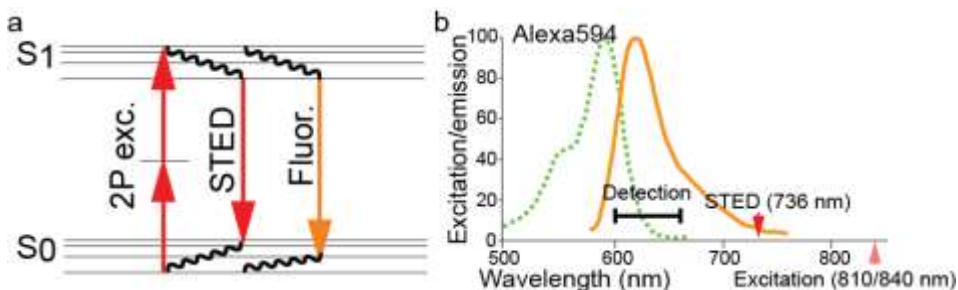


**Figure 2.1 a**, Energy level diagram illustrating the molecular transitions produced by the various wavelengths. The electronic ground and excited states, labeled  $S_0$  and  $S_1$ , respectively, are subdivided into sublevels accounting for vibronic and rotational energy. **b**, Excitation (*dashed green line*) and emission spectrum (*solid orange line*) for the soluble, organic dye, Alexa Fluor 594. The wavelengths used to produce two-photon excitation and STED, as well as the detection band, are labeled on the horizontal axis.

A crucial distinction between the two processes described in (2.1) that is particularly important for the observation of stimulated emission depletion (STED) is that stimulated emission produces “copies” of the incident photons and selectively amplifies

the stimulating field mode. This allows for spectral filtering of stimulated emission and separation of the fluorescence signal from the stimulated background (Figure 2.1 b).

### 2.2.2. Stimulated emission depletion

The STED process can be described by a system of differential equations accounting for the relevant molecular transitions, including vibrational relaxation of the ground state and excitation by the STED laser (Leutenegger et al., 2010). In the case that the excitation laser is delivered in a short pulse, as is the case for two-photon excitation, and the rate of vibrational relaxation is sufficiently fast to prevent re-excitation by the STED laser, the time evolution of the excited state population,  $P_{S1}(t)$ , due to fluorescence and stimulated emission can be written as

$$\frac{dP_{S1}}{dt} = -k_F P_{S1} - k_{sted} P_{S1} \quad (2.5)$$

in which  $k_F$  is the single molecule rate of spontaneous emission, and  $k_{sted} = \sigma_{sted} I$ , where  $I$  is the intensity of the STED laser and where  $\sigma_{sted}$  is the stimulated emission cross-section, which depends on the emissive properties of the fluorophore, the STED laser wavelength, and the alignment of the fluorophore transition dipole with the polarization of the laser. In the case of continuous wave (CW) STED, in which  $I$  is a time-independent constant, solving (2.5) for the fraction of fluorescence over the total emission,  $\eta(I) = F_{sted}/F_0$ , yields

$$\eta_{cw} = \frac{1}{1 + I/I_{sat}} \quad (2.6)$$

where  $I_{sat} = k_F/\sigma_{sted}$  is also known as the saturation intensity and is more generally defined as the intensity necessary to suppress 50% of the normal fluorescence, i.e.

$\eta(I_{sat}) = 0.5$ . In the particular case of CW STED, this definition of  $I_{sat}$  also implies that it is the intensity at which  $k_{sted} = k_F$ .

### 2.2.3. Resolution enhancement in STED microscopy

STED microscopy achieves superresolution by suppressing fluorescence with STED in a spatially structured illumination pattern surrounding the excitation volume, which permits fluorescence only from regions localized around zero intensity nodes. One commonly used pattern of illumination is the STED ring with a zero intensity node at its center (Figure 2.2 a).

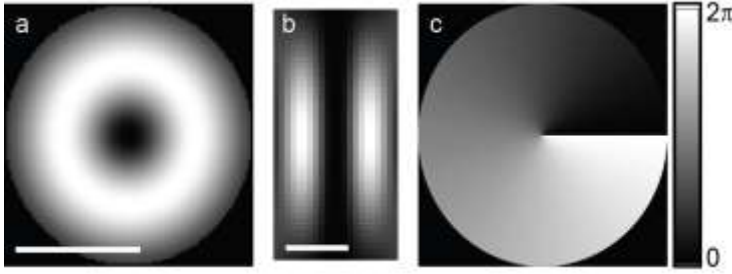


**Figure 2.2 a**, Simulated XY-cross-section of the STED ring illumination pattern in the focal plane. **b**, Simulated XZ-cross-section of the STED cylinder above and below the focal plane. **c**, Diagram of the vortex phase plate which imparts a helical wavefront to the STED beam. The resulting helical (Laguerre-Gaussian) beam produces the intensity pattern depicted in (a) and (b) after being focused through the objective. Scale bar is 500 nm.

Fluorescence suppression in this pattern reduces the apparent width of the PSF, enhancing lateral resolution, and the width of the PSF scales as

$$\Delta r_{sted} \approx \frac{\Delta r_0}{\sqrt{1 + I/I_{sat}}} \quad (2.7)$$

where  $\Delta r_0$  is the width of the conventional PSF without STED enhancement (Harke et al., 2008). According to (2.7), increasing the intensity of the STED laser reduces the width of

the PSF and enhances lateral resolution without limit. Because the STED ring forms a cylinder in 3-dimensions, the axial resolution is not improved (Figure 2.2 b).

#### 2.2.4. Theory of STED ring formation

The arbitrary illumination patterns used in STED microscopy can be practically implemented by controlling the wavefront and polarization of the laser beam entering the microscope objective (Keller et al., 2007). In the case of the STED ring, the initially collimated, linearly polarized STED laser is passed through a vortex phase plate producing a helical wavefront of topological charge 1 (Figure 2.2 c) and through a  $\lambda/4$ -wave plate oriented to produce circularly polarization with the same helicity as the wavefront. Accounting for vectorial diffraction allows numerical calculation of the electric field near the focus of the objective lens resulting from focusing a wavefront-shaped, polarized laser field described by the pupil function  $\vec{\mathbf{A}} = \begin{bmatrix} A_x \\ A_y \end{bmatrix}$ . The diffraction integral for the focused electric field at  $\vec{\mathbf{r}}'$  (primed coordinates referring to the 3-dimensional sample space whose coordinate origin is the focus, and unprimed coordinates referring to the 2-dimensional pupil space) is given by (Richards and Wolf, 1959),

$$\vec{\mathbf{E}}(\vec{\mathbf{r}}') = \int \sqrt{\cos \theta} \left( A_x \vec{\mathbf{K}}(\theta, \phi) + A_y \mathbf{R}_z\left(\frac{\pi}{2}\right) \vec{\mathbf{K}}\left(\theta, \phi - \frac{\pi}{2}\right) \right) \exp(iknr' \cos \varepsilon) \sin \theta d\theta d\phi \quad (2.8)$$

where  $\cos \varepsilon = \cos \theta \cos \theta' + \sin \theta \sin \theta' \cos(\phi - \phi')$ ,  $\mathbf{R}_z(\beta)$  is the coordinate rotation matrix through angle  $\beta$  around the z-axis, and

$$\vec{\mathbf{K}} = \begin{bmatrix} \cos \theta + (1 - \cos \theta) \sin^2 \phi \\ (\cos \theta - 1) \sin \phi \cos \phi \\ \sin \theta \cos \phi \end{bmatrix} \quad (2.9)$$

Numerically integrating (2.8) with an appropriate choice of the vectorial pupil function,  $\vec{A}$ , yields the electric field near the focus and enables simulation of the consequences of beam defects on the formation of the STED ring.

An important example of one such defect is improper polarization. As noted above, the beam must be circularly polarized with a handedness matching that of the helical wavefront (Iketaki et al., 2007). Circular polarization of the opposite spin leads to constructive interference of the axial field at the focus, producing a ring with a non-zero intensity center (Figure 2.3 a).

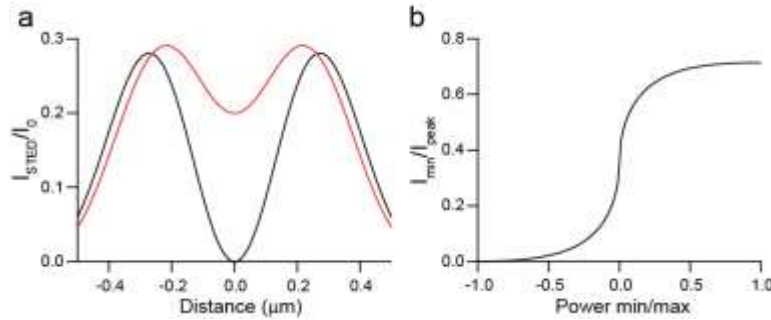


**Figure 2.3 a**, Simulated profile of the STED ring given a pupil field of proper (*black*) or improper (*red*) circular polarization. STED intensity ( $I_{\text{STED}}$ ) is normalized to the peak intensity of a normally focused beam of equal power ( $I_0$ ). **b**, Simulated intensity of the central minimum for varying pupil field polarization. -1, 0, and 1, denote proper circular polarization, linear polarization, and improper circular polarization, respectively, with continuously varying elliptical polarization between these values. STED minimum intensity ( $I_{\text{min}}$ ) is normalized to the peak intensity ( $I_{\text{peak}}$ ) of the proper STED ring in (a).

Numerical simulation of the dependence of the intensity of the central minimum on the polarization state of the beam shows that a zero intensity node is only formed with the proper circular polarization (Figure 2.3 b). Improper polarization diverts power into the central minimum, suppressing peak fluorescence and thereby reducing signal and degrading STED resolution. In the worst case of an oppositely polarized beam, an input intensity that would properly produce a modest 2-fold improvement in resolution leads to



a 70% reduction in peak fluorescence, while a proper 5-fold improvement results in a 95% loss of signal. Therefore, proper polarization of the STED beam is critical for achieving large enhancement factors.

Another important class of beam defects is the wavefront deformations associated with primary aberrations (Deng et al., 2010). Understanding the effects of primary aberrations on ring focusing is important to anticipating and diagnosing problems with STED imaging. The primary aberrations, spherical aberration, astigmatism, and coma, are commonly produced in uncorrected, low cost optics or through misalignment and improper use of optics. Coma is not usually of issue in a properly aligned microscope, and only the first two aberrations will be considered here. Astigmatism often results from the use of poor optics, particularly uncorrected scan lenses and objectives. Astigmatism in the pupil function results in an asymmetric ring with lobes along the axis of aberration (Figure 2.4 b).

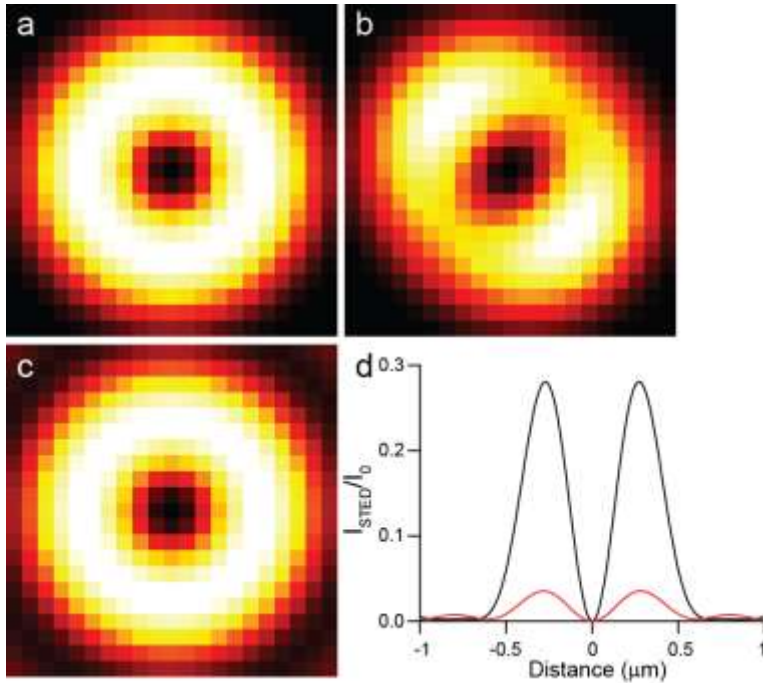


**Figure 2.4** **a**, Simulated intensity of the unaberrated STED ring. **b**, Simulated intensity of the STED ring with astigmatism. **c**, Simulated intensity of the STED ring with spherical aberration. **d**, Profiles of the STED ring intensity for unaberrated (*black*) and spherical-aberrated (*red*) focusing.

Strong astigmatism is of particular concern for STED imaging, as the asymmetry of the central minimum can lead to asymmetry in the PSF and differential resolution on the axes of aberration.

Spherical aberration is commonly encountered as a result of working with spherical lenses or through refractive index mismatching between the objective immersion medium and the sample. Spherical aberration in the pupil function results in a symmetric intensity profile (Figure 2.4 c) nearly identical to the properly formed ring (Figure 2.4 a). However, the peak intensity of the aberrated ring is drastically reduced, as the intensity profile becomes elongated along the z-axis. Spherical aberration is most clearly noted by the appearance of higher order rings visible as secondary lobes in 1-

dimensional profile (Figure 2.4 d). Though the geometry of the primary ring is left mostly intact, the reduced intensity leads to loss of STED resolution.

### **3. Two-photon excitation STED microscopy with continuous wave (CW) STED**

#### **3.1.Introduction**

The development of superresolution fluorescence imaging techniques described in 1.3 motivated exploration of the possibility of implementing superresolution two-photon microscopy for live imaging in tissue. The present chapter is a description of work demonstrating superresolution imaging in living brain tissue using STED microscopy implemented with a continuous wave (CW) laser in combination with 2PLSM (CW STED2P) (Ding et al., 2009).

#### **3.2.Design and operation of the CW STED2P microscope**

##### **3.2.1. Description of the microscope**

In order to explore the use of STED microscopy for superresolution fluorescence imaging in thick tissue, we designed and constructed a two-photon laser scanning microscope with an additional laser path for STED (Figure 3.1 a).

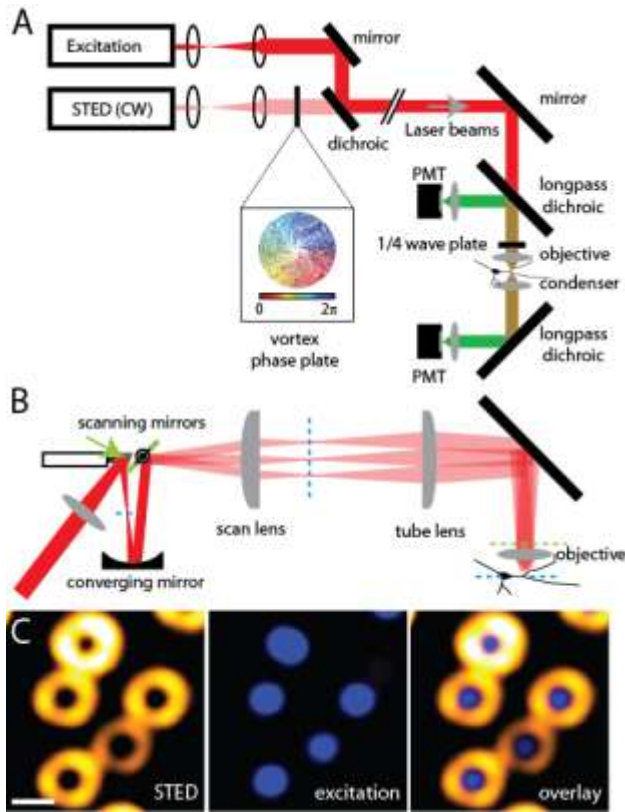


**Figure 3.1** **A**, Schematic of the optical path for modulation and combination of the two-photon excitation (*dark red*) and one-photon depletion (*light red*) laser light. The depletion laser beam is passed through a vortex phase plate ( $0 \leq \Phi \leq 2\pi$  phase modulation) before combination with the excitation light at a dichroic. Both epifluorescence and transfluorescence are collected by photomultiplier tubes (PMT). The  $\lambda/4$ -wave plate circularly polarizes the excitation and STED light. **B**, Schematic of the microscope scan head. This design places both scan mirrors and the back focal plane of the objective in conjugate optical planes and creates stationary illumination at the objective back aperture. The dashed blue lines indicate planes conjugate to the image whereas the dashed green lines and arrow represent planes conjugate to the objective back focal plane. **C**, 2PLSM images of crimson beads collected with the phase patterned depletion laser (left, *yellow*) and the excitation laser (middle, *blue*). The superposition of these (right) illustrates the annular distribution of depletion light in the focal plane around the excitation volume.

The imaging laser was a mode-locked Ti:Sapphire laser tuned to 840 nm, and the STED laser was a Ti:Sapphire laser operating in continuous wave mode at wavelengths of 736 nm and 760 nm for depletion of Alexa 594 and Crimson dyed polystyrene beads,

respectively. The outputs of the lasers were independently modulated with Pockel's cells and gated with mechanical shutters. After expansion and collimation, the laser outputs were combined using a dichroic mirror and directed through a planoconvex lens to a scanning galvanometer. The reflection from the galvanometer was directed to a curved silver mirror that recollimated the beams and imaged the first galvanometer onto the second. The scanning mirrors were imaged onto the back focal plane of the objective with a scan lens and tube lens.

Emitted fluorescence was collected by both epi and transfluorescence detectors. Shortpass dichroics and interference filters were used to eliminate excitation laser light. "Green" and "red" emitted photons were separated using a dichroic and barrier filters. Emitted photons were detected using photomultiplier tubes. The current output of the trans and epifluorescence detectors were combined at the input of trans-impedance preamplifiers.

Superresolution imaging with STED microscopy requires illumination of the specimen with a phase-patterned laser beam that selectively suppresses fluorescence from fluorophores located at the edges of the excitation volume. For this reason, STED microscopy requires that the phase of illumination be fixed in space and is not compatible with the non-stationary illumination of the back-focal plane of the objective found in most implementations of laser-scanning microscopes. We designed a laser scan head that produces stationary illumination of the objective back focal plane by making this plane optically conjugate to both scan mirrors (Figure 3.1 b). This was accomplished using a planoconvex lens and a curved silver mirror that maintain laser collimation while imaging one scanning galvanometer mirror onto the second. This optical arrangement

also improves laser power delivered into the objective by reducing the degree of overfilling of the back-aperture necessary to maintain imaging resolution.

### **3.2.2. Co-alignment of excitation and STED lasers**

In order to co-align the excitation and STED lasers, we prepared samples of 200 nm diameter Crimson beads suspended in ProLong Gold mounting media on glass slides. With the STED laser mode-locked and producing ~100 femtosecond pulses at 760 nm, we imaged Crimson beads by two-photon excitation generated fluorescence produced by the excitation laser at 840 nm and alternately by the STED laser at 760 nm. With the vortex phase plate placed in the STED laser path, two-photon excitation generated fluorescence from the Crimson beads produced fluorescence images of the excitation focus and the STED ring in alternate images, and visualization of the STED ring allowed spatial co-alignment of the excitation and STED lasers in the sample plane (Figure 3.1 c).

### **3.2.3. Two-photon excitation and CW STED of fluorescent dyes**

Proper co-alignment of the excitation and STED lasers enables suppression of fluorescence via CW STED of two-photon excitation generated excited states. To observe STED in practice, we removed the vortex phase plate and co-aligned the excitation and STED lasers to deplete in the entire focal volume. We first imaged 200 nm diameter polystyrene beads labeled with the red fluorescing organic dye, Crimson, with the excitation laser tuned to 840 nm (Figure 3.2 a).

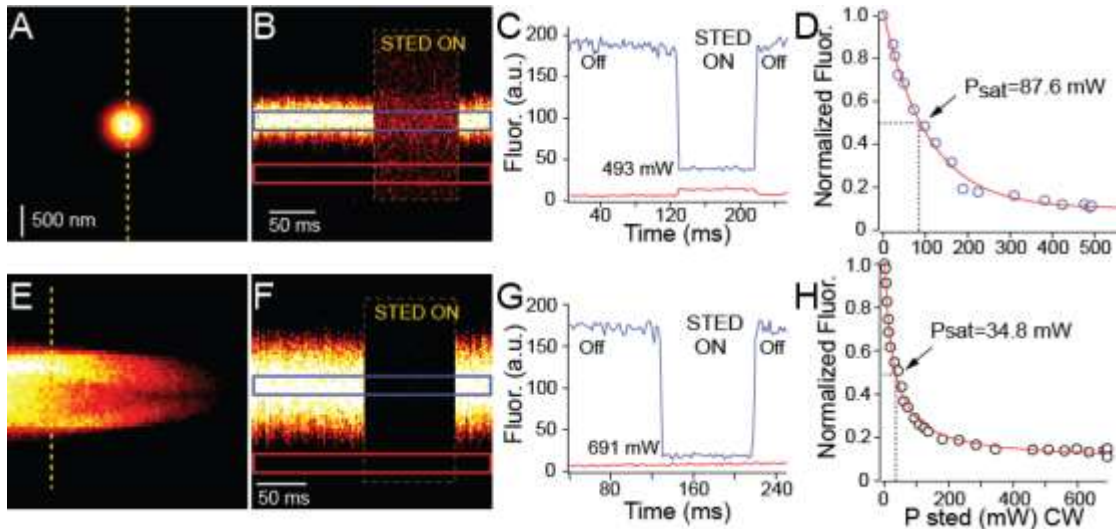


**Figure 3.2** **A**, Image of a 200 nm diameter Crimson fluorescent bead acquired with 2PLSM at excitation wavelength of 840 nm. **B**, Fluorescence measured in line scans over the region indicated by the dashed lines in (A) during normal excitation and with additional illumination with 760 nm light (boxed region). **C**, Quantification of fluorescence intensity in the regions of interest (ROI) indicated by the colored boxes in (B). Despite maintained 2-photon excitation, turning on the STED beam reduces fluorescence from the bead (*blue*). In addition, a small amount of background light is present (*red*) when the depletion laser alone is active. **D**, Relative fluorescence intensity of crimson fluorescent beads under 2-photon excitation at 840 nm as a function of the depletion laser power ( $P_{sted}$ ) at 760 nm. The power required for suppression of 50% of fluorescence is indicated. **E**, 2PLSM image of a sealed glass pipette filled with 50  $\mu\text{M}$  Alexa594 in aqueous solution. **F**, Fluorescence of Alexa594 measured in line scans over the region indicated by the dashed line in (E) during normal excitation and with additional illumination with CW 736 nm light (boxed region). **G**, Quantification of fluorescence intensity in the ROI indicated by the colored boxes in (F). **H**, Depletion of Alexa594 fluorescence under constant two-photon excitation with 840 nm light as a function of the power ( $P_{sted}$ ) of applied 736 nm depletion light.

Transient illumination with a second Ti:Sapphire laser operating in CW mode and tuned to 760 nm instantly and reversibly suppressed dye fluorescence in a power-dependent manner (Figure 3.2 b-c). The dependence of fluorescence on STED laser power was well fit by the expected rectangular hyperbola of the form,  $(1 + \gamma P_{STED})^{-1}$ . The power necessary



for 50% reduction of the fluorescence signal ( $P_{sat} = \gamma^{-1}$ ) was 87.6 mW measured at the back aperture of the objective (Figure 3.2 d).

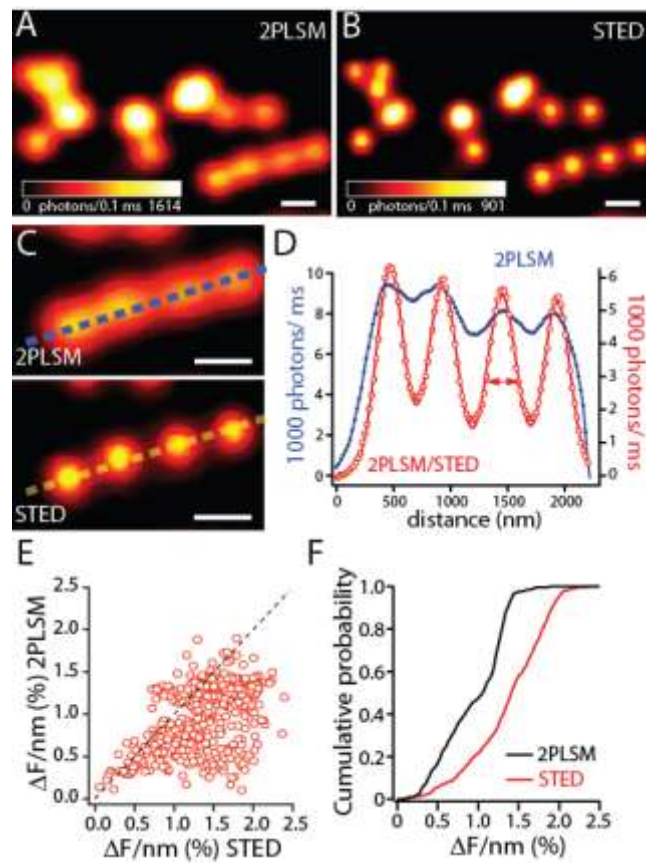
We also examined CW STED of a second, bright, highly soluble, fluorescent dye, Alexa Fluor 594, which is commonly used in live neuron filling for fluorescence imaging. Two-photon generated fluorescence from an aqueous solution of Alexa Fluor 594 (50  $\mu$ M) was imaged in a sealed glass pipette (Figure 3.2 e). Fluorescence was instantly and reversibly suppressed by simultaneous illumination with a CW laser tuned to 736 nm (Figure 3.2 f-g). The dependence of fluorescence on STED laser power was also well fit by the expected form,  $(1 + \gamma P_{STED})^{-1}$ , with a  $P_{sat}$  of 34.8 mW (Figure 3.2 h).

#### **3.2.4. CW STED2P imaging of fluorescent beads**

To demonstrate the superresolution capability of the CW STED2P microscope, we first imaged fluorescent beads of known size and shape. Introduction of the vortex phase plate and quarter wave plate ( $\lambda/4$ ) into the optical path produced the annular STED illumination pattern in the sample plane necessary for superresolution imaging (Figure 3.1 c). After co-aligning the excitation and STED lasers, we switched the STED laser into CW mode and imaged clusters of Crimson beads by 2PLSM with or without simultaneous illumination with the STED laser (Figure 3.3 a-b).

**Figure 3.3 A-B,** Images of fluorescent 200 nm crimson beads acquired with 2PLSM (A) and CW STED2P (B). The images were collected simultaneously by switching the STED laser on and off in alternate lines of the image at 500 Hz. **C,** Enlarged images of the linear cluster of beads in (A) and (B) acquired with (E) and without (F) the STED laser active. **D,** The profile of fluorescence intensity along the dashed lines in (C) exhibits clear separation of clustered fluorescent beads in the CW STED2P mode (*red*) but not in the 2PLSM mode (*blue*). The CW STED2P fluorescence profile was fit (*red line*) to the sum of four Gaussians with identical widths (FWHM = 300 nm) and a separation of 500 nm. **E,** Comparison of edge sharpness between 2PLSM image in (A) and 2PLSM/STED image in (B). To compare the resolution of structures imaged by 2PLSM or CW STED2P, every horizontal line profile in each images was used to calculate the maximal slope of bead edges. The maximal rate of change of fluorescence is expressed as a percent change per nm relative to total integrated fluorescence ( $\% \Delta F / \text{nm}$ ). For objects that can be accurately sampled by 2PLSM, the maximal rate of fluorescence change in the same when imaged by CW STED2P and the points should follow the dashed line ( $y=x$ ). In contrast, for structures that are below the resolution limit of 2PLSM, the rate of change of fluorescence increases under CW STED2P as indicated by the data points deviating from the dashed line. **F,** Cumulative distributions of maximal slopes obtained from 2PLSM (A) and CW STED2P (B) images. The application of STED to 2PLSM results in shifting and broadening of the distribution. The overall distribution shifted towards higher rates of fluorescence changes. Scale bars, 500 nm in all images.

Figure 3.3, Continued



Simultaneous illumination with the STED laser in CW mode reduced the width of the bead profiles and improved lateral resolution (Figure 3.3 c). Under conventional 2P imaging, fluorescence images of 200 nm diameter Crimson beads displayed an average full-width at half-maximum (FWHM) of 530 nm. In contrast, CW STED2P images exhibited an average FWHM of 280 nm, indicating a greater than 2-fold improvement in resolution. Likewise, CW STED2P improved the capability to resolve fluorescent structures in close proximity, including beads separated by less than 500 nm.

Lastly, the sharpness of the edges of beads, quantified by measuring the maximal rate of change of fluorescence in each line of the image, was greater for CW STED2P images than for conventional 2P images (Figure 3.3 e). The maximal slope of fluorescence in these images normalized by the cumulative fluorescence intensity ( $\% \Delta F / \text{nm}$ ) was larger for CW STED2P than for conventional 2P images, consistent with improved imaging resolution (Figure 3.3 f).

### **3.3.CW STED2P imaging in brain tissue**

#### **3.3.1. Consideration of refractive index mismatch**

To explore the potential for aberrations caused by refractive index mismatch between the immersion medium (water,  $\sim 1.34$ ) and brain tissue ( $\sim 1.41$ ), we imaged Crimson beads in poly-dimethyl siloxane (PDMS, Sylgard 184), which has a similar index of refraction ( $\sim 1.41$ - $1.43$ ) to that of brain tissue (Figure 3.4 a)(Yan et al., 2007). The annular distribution of the focused STED beam was maintained 200-250  $\mu\text{m}$  deep in PDMS without degradation of the zero-intensity center (Figure 3.4 b).

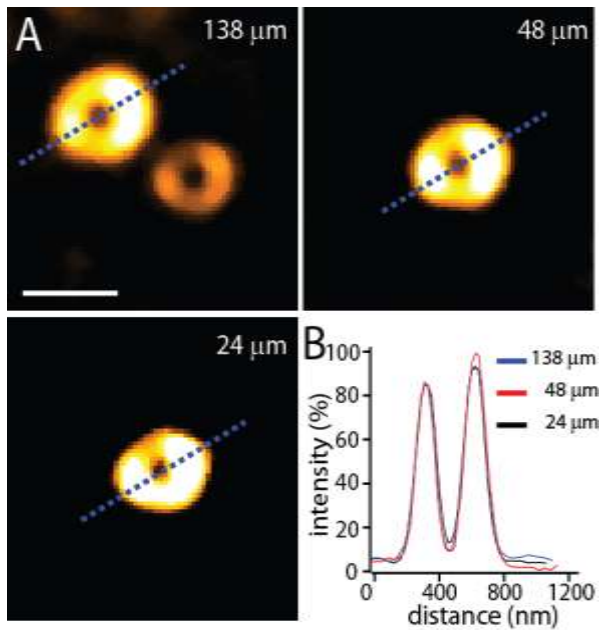


**Figure 3.4** **A**, 2PLSM imaging with the STED laser of crimson fluorescent beads embedded in PDMS demonstrates maintained formation of the annular illumination despite the index of refraction mismatch between the immersion solution and the PDMS. The depth of each bead below the surface of the PDMS block is indicated. **B**, The profiles of fluorescence intensity along the dashed lines in (A) indicate similar distributions at each depth.

### 3.3.2. Sample preparation, materials, and methods

To test the applicability of CW STED2P to live-cell imaging in brain tissue, we performed fluorescence imaging of CA1 hippocampal pyramidal neurons in mouse acute brain slices. Horizontal slices (300 μm thick) were cut from the hippocampus of 15-19-day-old C57BL6 mice in ice-cold ACSF containing (in mM): 125 NaCl, 2.5 KCl, 2 CaCl<sub>2</sub>, 1 MgCl<sub>2</sub>, 25 NaHCO<sub>3</sub>, 1.25 NaH<sub>2</sub>PO<sub>4</sub>, 25 glucose, bubbled with 95 % O<sub>2</sub> and 5 % CO<sub>2</sub>. After a 30 min incubation at 34 °C, slices were stored in ACSF at room temperature (22-23°C) until use. Individual slices were transferred to a submersion-style recording chamber and continuously superfused with ACSF at a rate of 2-3 ml/min at room temperature. Whole-cell voltage-clamp recordings were performed using standard

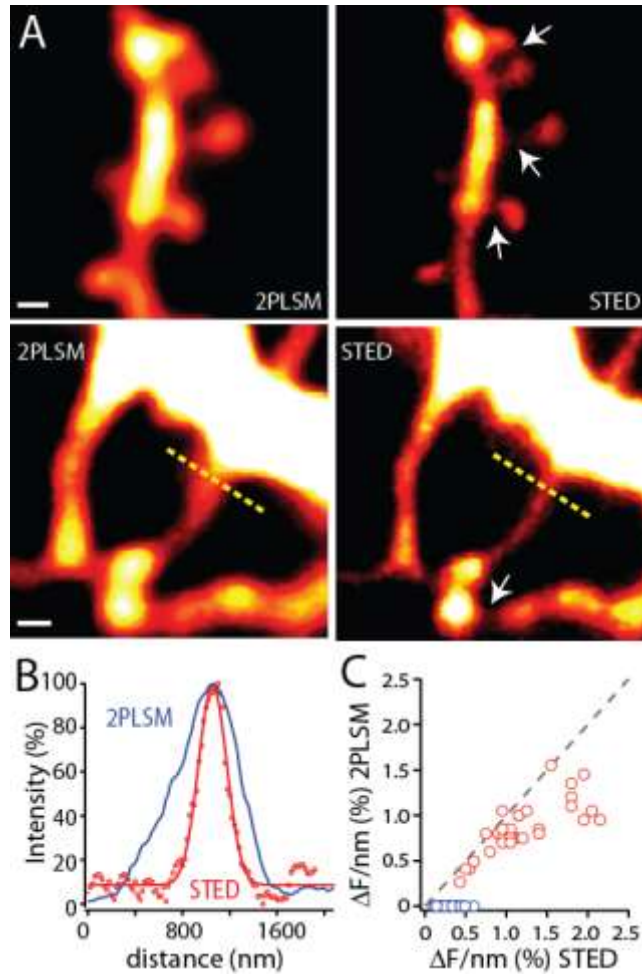
techniques. Recordings were performed on hippocampal CA1 pyramidal neurons visually identified in the slice with the help of infrared-differential interference contrast (IR-DIC) video microscopy with a Hamamatsu camera/controller system (Hamamatsu, Japan). Recording pipettes (3-5 M $\Omega$ ) were filled with Cs<sup>+</sup> internal solution containing the following (in mM): 120 CsMeSO<sub>3</sub>, 15 CsCl, 8 NaCl, 10 TEA-Cl, 10 HEPES, 2-5 QX-314, 0.2 EGTA, 2 Mg-ATP, 0.3 Na-GTP, pH 7.3 adjusted with CsOH. 100  $\mu$ M Alexa Fluor-594 was added in the internal solution for imaging of neuronal morphology.

### **3.3.3. Enhanced resolution of dendritic spines**

Neurons were filled with Alexa Fluor 594 (100  $\mu$ M) through a whole-cell patch clamp recording pipette and dendritic spines were imaged under conventional 2PLSM and CW STED2P imaging modes (Figure 3.5 a). For spines located 30-110  $\mu$ m below the surface of the slice, CW STED2P revealed significantly greater detail than conventional 2PLSM.

**Figure 3.5 A**, Image pairs of dendritic spines acquired with 2PLSM (left) and CW STED2P (right). CA1 pyramidal neurons in acute hippocampal slices were filled with 100  $\mu$ M Alexa 594 through a whole-cell recording pipette. The images were acquired simultaneously by switching the STED laser on and off in alternate lines at 500 Hz. The arrows indicate details in the STED image that are not resolved in 2PLSM. Scale bars, 500 nm in all images. The dendrites were located at approximate depths of 80  $\mu$ m (top) and 45  $\mu$ m (bottom) microns below the surface of the slice. **B**, The profiles of fluorescence intensity along the dashed lines in (A) demonstrate improved resolution of the spine neck in the CW STED2P mode (*red*) compared to in 2PLSM mode (*blue*). The line profile of spine neck in STED image was fit to a Gaussian with FWHM = 280 nm. **C**, Plot of the maximum rate of fluorescence changes in 2PLSM and CW STED2P images. In order to allow for comparison of images with different fluorescence intensities, the rate of change of fluorescence is expressed as a percent change per nm relative to total integrated fluorescence ( $\% \Delta F / \text{nm}$ ). For objects that can be accurately sampled by 2PLSM there should be no increase in the measured parameter when the same structure is imaged by CW STED2P. These points should lie along the line of unity (*dashed line*). In contrast, for structures that are below the resolution limit of 2PLSM, the rate of change of fluorescence should increase under CW STED2P as the blurring or low-pass filtering effect of low resolution is reduced. The blue points indicate regions of detail that are evident only in the CW STED2P images.

Figure 3.5, Continued





Improvements in resolution resulting from CW STED2P were evident from several features of the images. First, objects that appeared fused in 2PLSM were resolved as distinct objects by CW STED2P. This includes visualization of the separation between spine heads and parent dendrite, between closely spaced filopodia, and identification of multiple spines within indistinct fluorescence blobs. Second, the cross-sectional profile of thin objects such as filopodia was narrower in CW STED2P than in 2PLSM such that the full-width at half-maximum (FWHM) was reduced from 660 to 280 nm (Figure 3.5 b). Lastly, as revealed by the analysis of maximal rates of change of fluorescence described above, the sharpness of large objects such as mushroom spines and dendrites, was greater for CW STED2P than for 2PLSM images (Figure 3.5 c). This analysis indicates improved resolution that, as expected, is most evident for structures of high spatial frequency. The improved two-object discrimination and the increased sharpness of spine images as well as the FWHM of fluorescent beads were dependent on the STED illumination intensity, as expected for this imaging modality.

#### **3.3.4. Effect of lateral resolution enhancement on 3D reconstruction**

The vortex phase pattern implemented in CW STED2P improves resolution in lateral dimensions but not along the z-axis. In order to examine how CW STED2P affects resolution of 3D structures such as dendrites and spines, we analyzed 3D image stacks taken through fluorescent beads and spiny stretches of dendrite. Maximal intensity projections of 200 nm fluorescence beads again revealed improved resolution, reflected by decreased FWHM of the projected image from 420 nm to 240 nm (Figure 3.6 a).

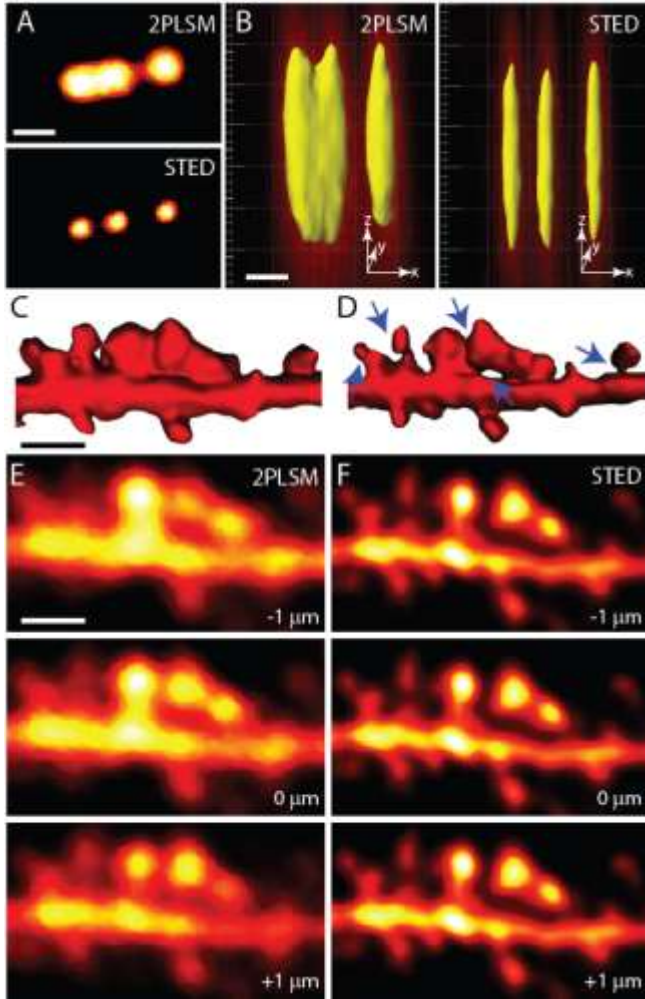


**Figure 3.6** **A**, Maximum intensity axial ('Z') projections of image stacks of fluorescent 200 nm crimson beads acquired with 2PLSM (top) and CW STED2P (bottom). Slice spacing = 200 nm. **B**, 3D reconstruction of the beads shown in (A). The 2PLSM images of the leftmost beads are fused along the entire Z-extent of the image stack whereas they are clearly distinct throughout the stack in the CW STED2P images. **C-D**, 3D surface rendering of a segment of dendrite and spines collected as an image stack (500 nm spacing, 12 slices) acquired with 2PLSM (C) and CW STED2P (D). The arrows indicate details in the STED rendering that are not resolved in 2PLSM. These include features of the spine heads, separations between structures, and spine necks. **E-F**, Sample individual slices of the image stack rendered in (C and D) acquired at different focal planes with 2PLSM (E) and CW STED2P (F). Scale bars, 500 nm in (A) and (B), 2 μm in (C-F).

Furthermore, surface rendering of the 3D image stack confirmed that the reduced fluorescence spread with CW STED2P was maintained in out-of-focus planes, allowing

improved separation of objects throughout their 3D extent (Figure 3.6 b). Similar surface rendering of deconvolved image stacks of spiny regions of dendrite indicated improved discrimination of morphological features including the ability to distinguish tightly packed structures and resolve spine necks (Figure 3.6 c-d). Furthermore, even within this highly complex 3D fluorescence distribution the increased resolving power of CW STED2P allowed improved identification of morphological features within each plane of the raw image stacks (Figure 3.6 e-f).

### **3.3.5. Use of CW STED2P for morphological analysis**

To further quantify the ability of CW STED2P to resolve the fine features of dendrites of living neurons, we measured the dimensions of dendritic spines in 3D image stacks acquired by conventional 2PLSM and by CW STED2P. As expected, greater morphological detail of spines was clearly visible in maximal intensity projections of highly spiny dendritic regions (Figure 3.7 a).

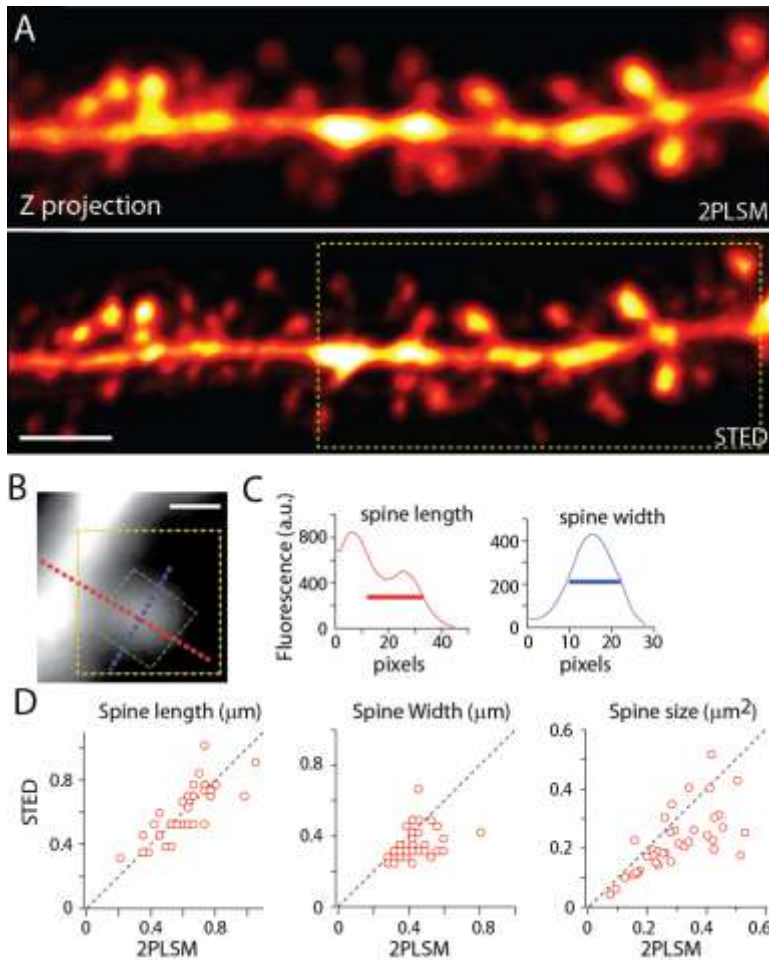


**Figure 3.7** **A**, Maximum intensity projection of image stacks of dendrite and spines acquired with 2PLSM (top) and CW STED2P (bottom). Scale bars, 2  $\mu\text{m}$ . **B**, Image of an individual dendritic spine indicating the method of morphometric analysis. The major (*red line*) and intersecting minor (*blue line*) axes were marked along the length and the width of the spine. The green box indicates the area containing the spine head. The pixels within this box whose fluorescence intensities are at least 50% of the maximal value are used to define the area of the spine head. Scale bars, 500 nm. **C**, The distances to 50% of maximal fluorescence along the major and minor axis were used to define, respectively, the apparent spine length (thick red line) and head width (thick blue line). **D**, Comparison of spine length (left), head width (middle), and head area (right) measured from images shown in A collected with CW STED2P (y-axis) and 2PLSM (x-axis). The spine lengths are similar in both imaging modes whereas the head widths and areas are smaller with CW STED2P than with 2PLSM.

For each spine, the spine length, spine head width, and spine head cross-sectional area were measured (Figure 3.7 b-c). Dimensions that are accurately captured by conventional

2PLSM are expected to be quantitatively unchanged under CW STED2P, whereas those that are significantly blurred by 2PLSM should appear smaller with CW STED2P. For each spine (n=36), length was similar under 2PLSM and CW STED2P (CW STED2P length =  $650 \pm 35$  nm; 2PLSM length =  $649 \pm 35$  nm,  $p > 0.05$ ; Wilcoxon signed-rank) whereas the spine head width (CW STED2P width =  $366 \pm 15$  nm; 2PLSM width =  $436 \pm 17$  nm,  $p < 0.001$ ; Wilcoxon signed-rank) and area (CW STED2P area =  $0.22 \pm 0.02$   $\mu\text{m}^2$ ; 2PLSM area =  $0.30 \pm 0.02$   $\mu\text{m}^2$ ,  $p < 0.0001$ ; Wilcoxon signed-rank) were significantly less with CW STED2P (Figure 3.7 d). In addition, compared to conventional 2PLSM, under CW STED2P the fluorescence intensity of spine heads relative to that of the dendrite increased 23.2%, as expected for small structures imaged with improved resolution (CW STED2P spine head/dendrite fluorescence ratio =  $0.35 \pm 0.17$ ; 2PLSM  $0.30 \pm 0.18$ ,  $p < 0.0001$ ; Wilcoxon signed-rank). Thus, the improved lateral resolution of CW STED2P significantly increases the ability to measure dimensions of dendritic spines in brain slices.

### **3.3.6. Consideration of phototoxicity of STED imaging in tissue**

Since CW STED2P requires using relatively high powers of CW laser light, we examined if phototoxicity would prevent repetitive time-lapse imaging of the same dendrite. The images show typical results of seven repeated images of the same dendritic region taken quickly over an 8 minute time window with 2PLSM and CW STED2P (Figure 3.8).

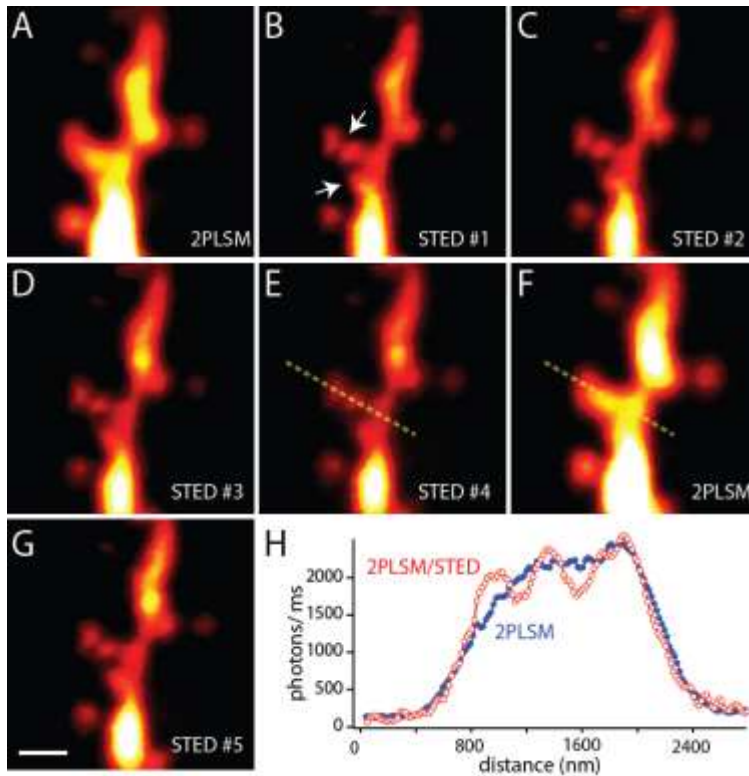


**Figure 3.8** **A-G**, Multiple images of an Alexa 594 loaded dendritic segment acquired with 2PLSM (**A** and **F**) and CW STED2P (**B-E** and **G**). The arrows indicate details in the CW STED2P image that are repeatedly resolved despite prolonged imaging. Scale bars: 1  $\mu\text{m}$ . The dendrite was at an approximate depth of 80  $\mu\text{m}$  in the slice. **H**, The profile of fluorescence intensity along the dashed lines in (**E**) and (**F**) exhibits clear separation of clustered spines in the CW STED2P mode (red) but not in the 2PLSM mode (blue).

No evidence of photodamage was detectable, and all CW STED2P images consistently exhibited separation of clustered spines that were not resolvable by 2PLSM. Furthermore, since the fluorophore in these experiments is a freely diffusing small molecule, photobleaching of the structure is not evident over time. Lastly, quantitative analysis of spine morphology during repetitive imaging at 1 minute intervals revealed little change in spine length, head width, and head cross-sectional area over time, consistent with a lack of significant photodamage (Figure 3.9).

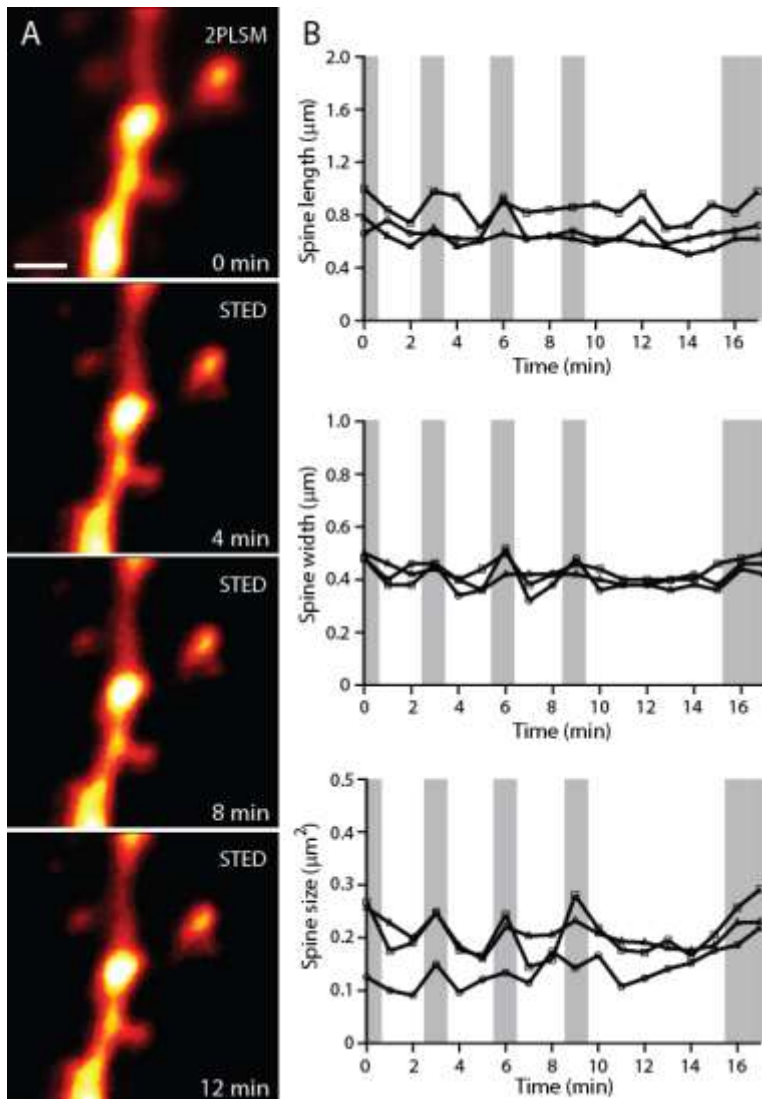


**Figure 3.9** **A**, The indicated small section of dendrite was imaged repeatedly with 2PLSM and full STED laser power over time and spine dimensions were measured as in Figure 6. Scale bar: 1  $\mu\text{m}$ . **B**, Despite the intense laser power delivery to this small region, the spine lengths (top), head widths (middle), and head areas (bottom) were stable over time, indicating lack of photodamage. The low motilities of these structures are as expected for neurons under whole-cell recording conditions. At the times indicated in gray, the STED laser was switched off and a standard 2PLSM image was collected.

### 3.4. Discussion

The findings in this chapter demonstrate that CW STED2P is capable of enhancing resolution of two-photon fluorescence imaging of neuronal structures deep in brain tissue.

In our experiments, ~3 fold improvement in radial resolution was achieved when imaging at depths of ~100 microns in brain slices. The utility of STED2P for deep tissue imaging arises from the use of multiphoton excitation and near infrared light. Here, we have demonstrated that, in practice, spherical aberrations due to index of refraction mismatches, forward scatter of excitation photons, and phototoxicity are not significant obstacles to the implementation of STED2P.

In addition, we found that Alexa Fluor 594, a bright fluorophore commonly used in live cell and fixed tissue imaging, is suitable for STED2P. Alexa Fluor 594 has a low  $I_{sat}$  for CW STED such that, with our currently available laser power,  $I_{max}/I_{sat} = \sim 6$  which predicts a 2- to 3-fold improvement in resolution. We also found that CW STED2P with Alexa 594 is suitable for repeated time-lapse imaging with minimal photobleaching and no visible photodamage. This is particularly important because, as the volume of excited fluorophores is reduced in STED imaging, the number of emitted photons is decreased and increased excitation laser power or averaging is required to maintain signal-to-noise ratios. Since Alexa 594 is an exceptionally bright and stable fluorophore, high-quality CW STED2P images can be achieved with low concentrations of fluorophore that are compatible with live cell imaging.



## **4. Two-photon excitation STED microscopy with pulsed STED**

### **4.1.Introduction**

In the previous chapter, STED microscopy was successfully combined with 2PLSM (STED2P) to achieve superresolution imaging of two-photon generated fluorescence in living tissue. The demonstration of 5-fold enhancement of two-photon imaging resolution in fixed cultured cells(Moneron and Hell, 2009) and the requirement for sub-100 nm resolution to produce accurate images of dendritic spine morphology motivated further development of STED2P imaging in brain tissue.

The present chapter is a description of work demonstrating superresolution imaging in living brain tissue with sufficient resolution to accurately image dendritic spine morphology using a combination of 2PLSM and STED microscopy implemented with laser pulses(Takasaki et al., 2013). Generally, pulsed STED will produce greater fluorescence suppression over CW STED given the same time-averaged power(Willig et al., 2007), as illustrated in Figure 4.1.

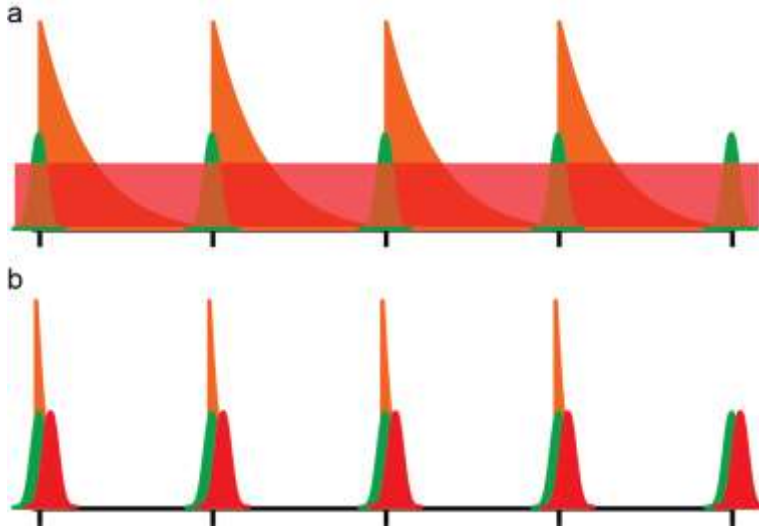


**Figure 4.1 a**, Diagram illustrating CW STED2P imaging cycle. Two-photon excitation pulses (*green*) arrive every 12 ns and drive fluorophores into the excited state from which they spontaneously decay to the ground state over time producing fluorescence (*orange*). The CW STED laser is applied continuously (*red*). **b**, Diagram illustrating STED2P with a pulsed STED laser (*red*) phase-locked to excitation (*green*). Compression of laser power into pulses with precisely timed delivery enhances suppression of fluorescence (*orange*).

Thus, pulsed STED2P (pSTED2P) should exhibit better fluorescence suppression and better resolution for the same average power. Temporal compression amplifies pulse intensity, enhancing fluorescence suppression (Figure 4.1 b), as well as the probability of two-photon excitation by the STED laser. Consequently, the optimal width of near-infrared STED pulses is bounded from below by the nonlinearity of two-photon excitation and bounded from above by the graded decrease in depletion efficiency toward the CW limit.

## 4.2. Design and operation of the pSTED2P microscope

### 4.2.1. Description of the microscope

In order to achieve fluorescence imaging of living neurons in an acute brain slice with better than 100 nm resolution, we constructed a two-photon laser scanning microscope

incorporating pulsed stimulated emission depletion (STED) of fluorescence produced by two-photon excitation (Figure 4.2).

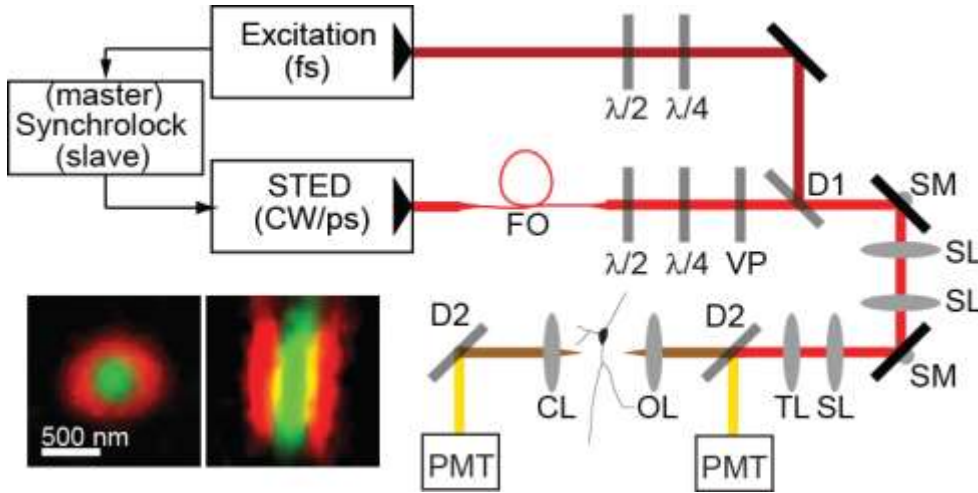


**Figure 4.2** Laser pulses from a femtosecond-pulsed Ti:Sapph laser (Excitation) for two-photon excitation (2PE) are synchronized by an electronic feedback circuit (Synchrolock) with a picosecond-pulsed Ti:Sapph laser (STED) for stimulated emission. STED pulses are stretched to  $\sim 200$  ps by dispersion through a 120 m single-mode polarization-maintaining fiber optic (FO) and phase patterned to achieve a helical wavefront by a vortex phase plate (VP). The 2PE and STED lasers are combined by a dichroic (D1). Fluorescence is separated from excitation and depletion light by a dichroic (D2) and collected by photomultiplier tubes (PMT).  $\lambda/2$  and  $\lambda/4$  are half- and quarter-waveplates used to adjust the polarization and compensate for down-stream elements in the scan head, such as dichroics, that perturb the polarizations of the excitation and depletion light. SL: Scan lens, TL: Tube lens, SM: Scanning mirror, Obj: Objective. *Inset*: Visual alignment of 2PE and STED foci by fluorescence imaging of quantum dots (Qdot605, Invitrogen). Composite imaging of the 2PE point-spread function (PSF) and STED PSF allows spatial coalignment in the XY (*left*) and XZ (*right*) planes.

Two-photon excitation was produced by  $\sim 200$  femtosecond laser pulses at 80 MHz repetition rate from a mode-locked Ti:Sapphire laser (Chameleon, Coherent, Santa Clara, CA). STED laser light was produced by a second Ti:Sapphire laser (Mira-HP, Coherent) generating pulses of  $\sim 2$  picosecond duration at wavelengths of 736 nm and 760 nm for

depletion of Alexa Fluor-594 (Life Technologies, Grand Island, NY) and Crimson (Life Technologies), respectively. To prevent two-photon excitation by the STED laser at high depletion powers, STED pulses were further stretched from ~2 picosecond to ~200 picosecond by dispersion through 120 meters of polarization-maintaining single-mode fiber optic (PM-S630-HP, Thorlabs, Newton, NJ). The outputs of both lasers were independently modulated with Pockel's cells (350-80, Conoptics, Danbury, CT) and gated with mechanical shutters (VS25S2ZM1 and LS6Z2, Uniblitz, Vincent Associates, Rochester, NY). The STED laser was directed through a vortex phase plate (VPP-2, RPC Photonics, Rochester, NY) producing a helical wavefront to form the annular intensity distribution in the specimen plane. The lasers were combined using a dichroic mirror (800SP, Chroma, Bellows Falls, VT) and coaligned at the sample plane by simultaneous 2P imaging of quantum dots (QDot 605, Life Technologies; ~20 nm diameter). Point-scanning was achieved by a symmetric pair of scanning galvanometers (6215H, Cambridge Technology, Cambridge, MA). The x-axis scan mirror was imaged by a pair of scan lenses (FV-PL-5I, Olympus) onto a second identical galvanometer oriented on an orthogonal axis to produce raster scanning of the sample. The scanning mirrors were imaged onto the back aperture of the objective (60x, 1.1NA, LUMFL N, Olympus, Melville, NY) with a scan lens (FV-PL-5I, Olympus) and an achromatic tube lens (AC254-200-B, Thorlabs). This optical arrangement places both scan mirrors and the back aperture of the objective in conjugate optical planes, creating stationary illumination at the objective back aperture and preserving the STED annulus across the scan field. Both laser beams were circularly polarized by passage through a combination of half- and quarter-wave plates (10RP42 and 10RP44, Newport, Irvine, CA).

Emitted fluorescence was collected by epi- and trans-fluorescence detectors. Shortpass dichroics (700DCXR, Chroma) and interference filters (E700SP-2P) were used to eliminate excitation and depletion laser wavelengths. Green and red channels were separated using a dichroic (565DCXR, Chroma) and barrier filters (green: 525/50, red: 630/69, Semrock, Rochester, NY). Emitted photons were detected using photomultiplier tubes (H10770P-40MOD, Hamamatsu, Hamamatsu City, Japan). No pinhole was placed in the collection path.

Imaging and physiology data were acquired using National Instruments data acquisition boards and modified versions of ScanImage(Pologruto et al., 2003) written in MATLAB (MathWorks, Natick, MA). STED laser powers were measured at the output of the microscope objective. Live neuron imaging was performed with a time-averaged STED power of ~52 mW. Off-line analysis was performed using custom routines written in MATLAB and ImageJ. Pixel size was measured by translation of a dye filled, sealed pipette tip across the field of view with a calibrated micromanipulator, and independently confirmed by similar measurements using large, isolated fluorescent beads of 1  $\mu\text{m}$  diameter (Yellow-Green FluoSpheres, Life Technologies). The pixel size of all images was  $18 \times 18$  nm, and the pixel dwell time was 8  $\mu\text{s}$ , unless stated otherwise. Fitting and measurement were performed on raw image data, unless specified otherwise. Background subtraction and median filtering was applied to example images for display. Background subtraction of STED laser light from STED2P images was achieved by acquiring a background image produced by the STED laser alone, mean filtering, and then subtracting the background image from the raw STED2P image.

#### 4.2.2. Co-alignment of excitation and STED laser pulses

Two-photon imaging of bright quantum dots allowed for direct visualization of the STED laser focus and precise spatial coalignment of the excitation and STED lasers (Figure 4.2 inset). Pulse trains from the excitation and depletion lasers were synchronized and delay adjusted to produce maximal depletion by an electronic control circuit (Synchrolock, Coherent).

#### 4.2.3. Demonstration and characterization of pulsed STED

To demonstrate the ability of the microscope to suppress fluorescence by pulsed STED, we imaged a sealed glass pipette containing Alexa Fluor 594 (A594) by two-photon excitation with the excitation laser tuned to 810 nm and with the vortex phase plate removed from the optical path, briefly illuminated the pipette with STED laser pulses centered on 736 nm (Figure 4.3 a-b). By varying the relative delay between the excitation and STED pulse trains, we observed that the efficiency of depletion depended on the timing interval between the pulse arrivals (Figure 4.3 c) in a manner consistent with STED produced by a ~200 picosecond pulse. To computationally simulate the relationship between depletion efficiency and pulse timing, numerical integration of the following differential equation for the rate of fluorescence was performed in MATLAB

$$\frac{dF}{dt} = k_F N(t) \quad (4.1)$$

where  $k_F$  represents a monoexponential spontaneous emission process, and  $N(t)$  is the population of the fluorescent state. Interaction with a STED pulse was modeled through coupling of the fluorescent state to a second, time-dependent decay pathway, obeying the following

$$\frac{dN}{dt} = -(k_F + k_S(t))N(t) \quad (4.2)$$

$k_S(t)$  was modeled as a Gaussian pulse of temporal duration  $2\sigma$  and offset  $\tau$ .

Depletion efficiency was quantified by the STED laser power needed to suppress 50% of fluorescence,  $P_{sat}$ , which is related to  $I_{sat}$  in Eq.1 by a factor determined by the spatial geometry of the microscope focus. Comparison of depletion efficiency by mode-locked and CW output produced by the same STED laser demonstrated an  $\sim 7$ -fold enhancement by pulsed depletion (Pulsed  $P_{sat} = 1.0$  mW, CW  $P_{sat} = 7.2$  mW; Figure 4.3 d).

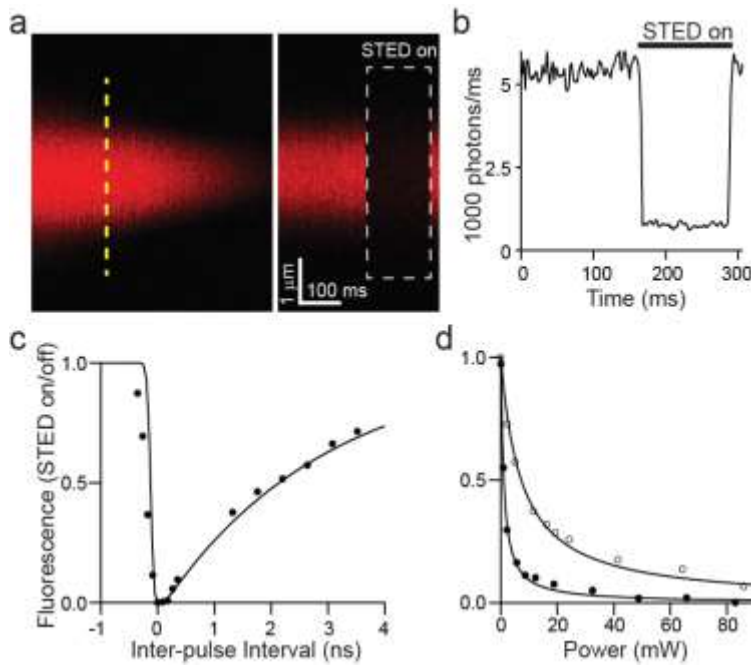


**Figure 4.3** **a**, 2PLSM image ( $\lambda_{exc}=810$  nm) of sealed glass pipette containing a solution of the red fluorophore Alexa Fluor-594 (*left*) and fluorescence collected in linescan mode (*right*) along the dashed line. During the time indicated by the boxed white region, the pulsed STED laser light was delivered ( $\lambda_{sted}=736$  nm), suppressing fluorescence. For these experiments, the vortex phase plate was withdrawn from the STED path to deplete the entire excitation volume. **b**, Fluorescence in the pipette measured in linescan (**a**) before, during, and after pSTED illumination, demonstrating reversible suppression of fluorescence. **c**, Fluorescence depletion efficiency, quantified as the ratio of fluorescence with and without pSTED illumination plotted against the relative timing delay between

excitation and STED pulses. Depletion efficiency versus relative timing was numerically simulated for a 200 ps STED pulse (*solid line*). **d**, Depletion efficiency versus STED laser power for pulsed (*filled circles*) and continuous wave (*open circles*) depletion modes. Data points were fit to rectangular hyperbolas to determine the power producing 50% depletion ( $P_{sat}$ ).

#### **4.2.4. Interaction of excitation and STED laser polarization**

The rate of stimulated emission depends on the alignment of the transition dipole with the electric field which implies that depletion efficiency may be sensitive to STED laser polarization if molecular alignment is anisotropic. Two-photon excitation may transiently produce a more polarized population of excited fluorophores than excitation by one-photon absorption, which could affect depletion efficiency by STED pulses of different polarizations (A. J. Bain et al., 2008). We measured depletion efficiency of Alexa Fluor 594 in both the pulsed and CW cases with parallel and orthogonal relative polarizations of the excitation and STED lasers (Figure 4.4 a).



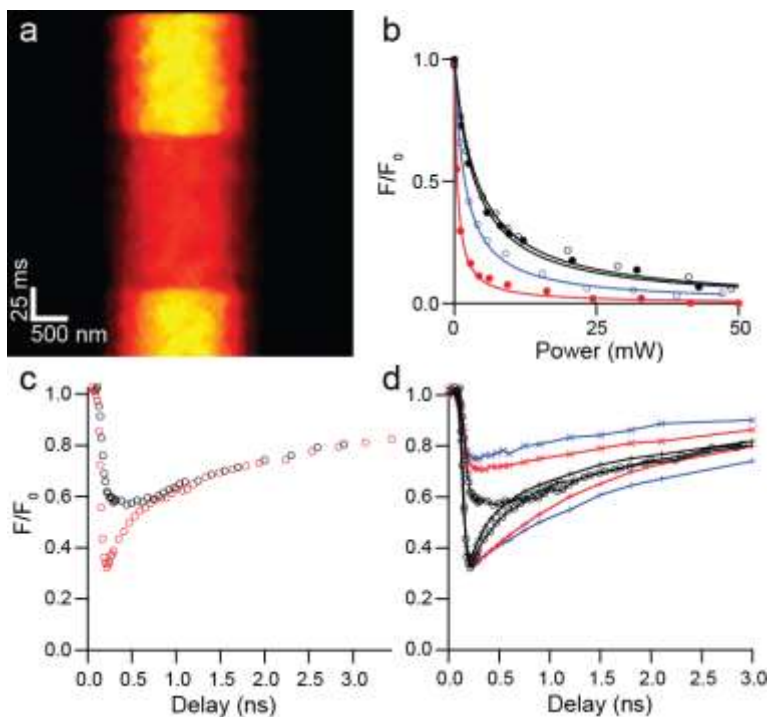


**Figure 4.4 a**, Line scan through a sealed glass pipette containing Alexa Fluor 594 with transient STED illumination. **b**, Depletion efficiency versus STED laser power for parallel (*filled circles*) and orthogonal (*open circles*) relative polarizations in pulsed (*red/blue*) and continuous wave (*black*) depletion modes. Data points were fit to rectangular hyperbolas to determine the saturation intensity producing 50% depletion. **c**, Delay-dependence of fluorescence suppression for parallel (*red*) and orthogonal (*black*) relative polarization. **d**, Delay-dependence and polarization anisotropy of Alexa 594 dissolved in pure water (*black*), 25% glycerol (*red*), and 50% glycerol (*blue*), for parallel (+ markers) and orthogonal (x markers) relative polarization.

Excitation and depletion with parallel linear polarization demonstrated better depletion efficiency over orthogonal polarizations (parallel  $I_{\text{sat}} = 1.0 \pm 0.05$  mW; orthogonal  $I_{\text{sat}} = 3.6 \pm 0.03$  mW), but had a much weaker effect on the efficiency of CW depletion (parallel  $I_{\text{sat}} 7.0 \pm 0.3$  mW; orthogonal  $I_{\text{sat}} 7.9 \pm 0.4$  mW) (b). Considering that pulsed STED is far more sensitive than CW STED to the relative polarizations of the excitation and STED lasers, one possibility is that relaxation of net molecular alignment produced by two-photon excitation occurs on time scales similar to that of the STED pulse width. To

determine whether a time-dependent relaxation process could be involved, we measured fluorescence suppression as a function of the timing delay between excitation and STED pulses (Figure 4.4 c). A clear dip in fluorescence suppression by para-polarized excitation and STED lasers was evident on timescales of ~500 ps. The duration of the dip was prolonged in solutions of pure water mixed with glycerol (Figure 4.4 d), suggesting that viscosity may influence the rate of equilibration of molecular alignment.

#### **4.2.5. pSTED2P imaging of 40 nm fluorescent beads**

To demonstrate superresolution imaging of targets of known shape and to estimate the increase in resolution achievable by pulsed STED 2PLSM (pSTED2P) for a particular fluorophore, we imaged 40 nm diameter polystyrene beads containing “Red” fluorescent dye (Figure 4.5 a).

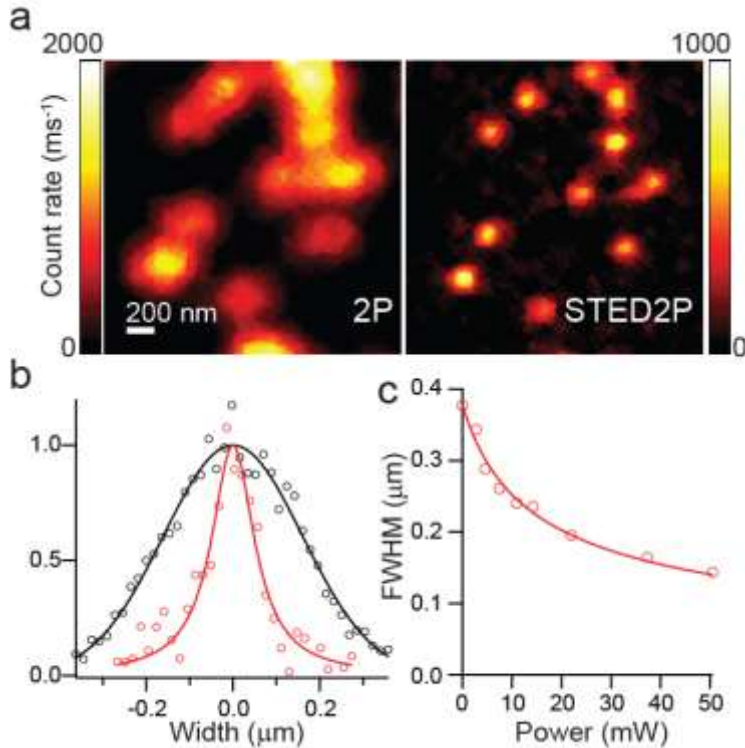


**Figure 4.5 a**, Images of 40 nm Red fluorescent beads with conventional 2PLSM (*left*) and pulsed STED 2PLSM (*right*). **b**, Line profile of bead fluorescence measured across an isolated bead in (a) by 2PLSM (*black markers*) and pSTED 2PLSM (*red markers*). 2P data were fit by a Gaussian (FWHM=377 nm) and pSTED2P data were fit by a Lorentzian (FWHM=144 nm). **c**, FWHM of pSTED2P images of isolated beads plotted against STED power. Bead profiles were fit with Gaussian and Lorentzian functions, and the FWHM was determined from the function producing the best fit. Data points were fitted to the inverse square-root function in Eq.1 (*solid line*).

40 nm diameter microspheres labeled with Red fluorescent dye (Red FluoSpheres, Life Technologies) were prepared in ProLong Gold mounting media on glass coverslips and mounted on a glass slide. Analysis of bead fluorescence demonstrated a nearly 3-fold improvement in resolution as measured by the widths of bead images (2P FWHM = 377 nm; pSTED2P FWHM = 144 nm) (Figure 4.5 b) with pulsed depletion. The dependence of bead image width on STED power was well fit by the inverse square-root relation ((2.7); Figure 4.5 c). The value of  $P_{sat}$  derived from the fit to the image data ( $P_{sat} = 2.41 \pm 0.24$  mW) was in agreement with the value determined from depletion curves

measured with 1  $\mu\text{m}$  diameter Red fluorescent beads ( $P_{\text{sat}} = 2.44 \pm 0.10$  mW; data not shown), demonstrating STED resolution enhancement in accord with theoretical expectations.

### **4.3.pSTED2P imaging in brain tissue**

#### **4.3.1. Sample preparation, materials, and methods**

To characterize enhancement in resolution of small structures embedded in living tissue, we imaged dendritic spines of CA1 pyramidal neurons in the native brain tissue of a 300 micron thick acute slice. Horizontal slices 300  $\mu\text{m}$  thick were cut from the hippocampus of 15-19 day-old C57BL6 mice in ice-cold ACSF containing (in mM): 125 NaCl, 2.5 KCl, 2 CaCl<sub>2</sub>, 1 MgCl<sub>2</sub>, 25 NaHCO<sub>3</sub>, 1.25 NaH<sub>2</sub>PO<sub>4</sub>, 25 glucose, bubbled with 95 % O<sub>2</sub> and 5 % CO<sub>2</sub>. After a 30 min incubation at 34 °C, slices were stored in ACSF at room temperature (22-23°C) until use. Individual slices were transferred to a submersion-style recording chamber and continuously superfused with ACSF at a rate of 2-3 ml/min at room temperature. Whole-cell recordings were obtained from hippocampal CA1 pyramidal neurons visually identified in the slice by Dodt contrast video microscopy with a camera and controller system. Recording pipettes (1-3 M $\Omega$ ) were filled with Cs<sup>+</sup> internal solution containing the following (in mM): 120 CsMeSO<sub>3</sub>, 15 CsCl, 8 NaCl, 10 TEA-Cl, 10 HEPES, 2-5 QX-314, 0.2 EGTA, 2 Mg-ATP, 0.3 Na-GTP, pH 7.3 adjusted with CsOH. 500  $\mu\text{M}$  Alexa Fluor-594 was added in the internal solution for imaging of neuronal morphology. Individual cells were filled with A594 through a whole-cell recording electrode under conditions identical to those used for electrophysiological analysis of neuronal function.

### 4.3.2. Comparison of CW and pulsed STED resolution

To examine the enhancement in resolution afforded by the improved depletion efficiency of pulses over CW STED, the same dendritic spines were imaged by pSTED2P and by CW STED2P under identical time-averaged STED power (Figure 4.6 a).

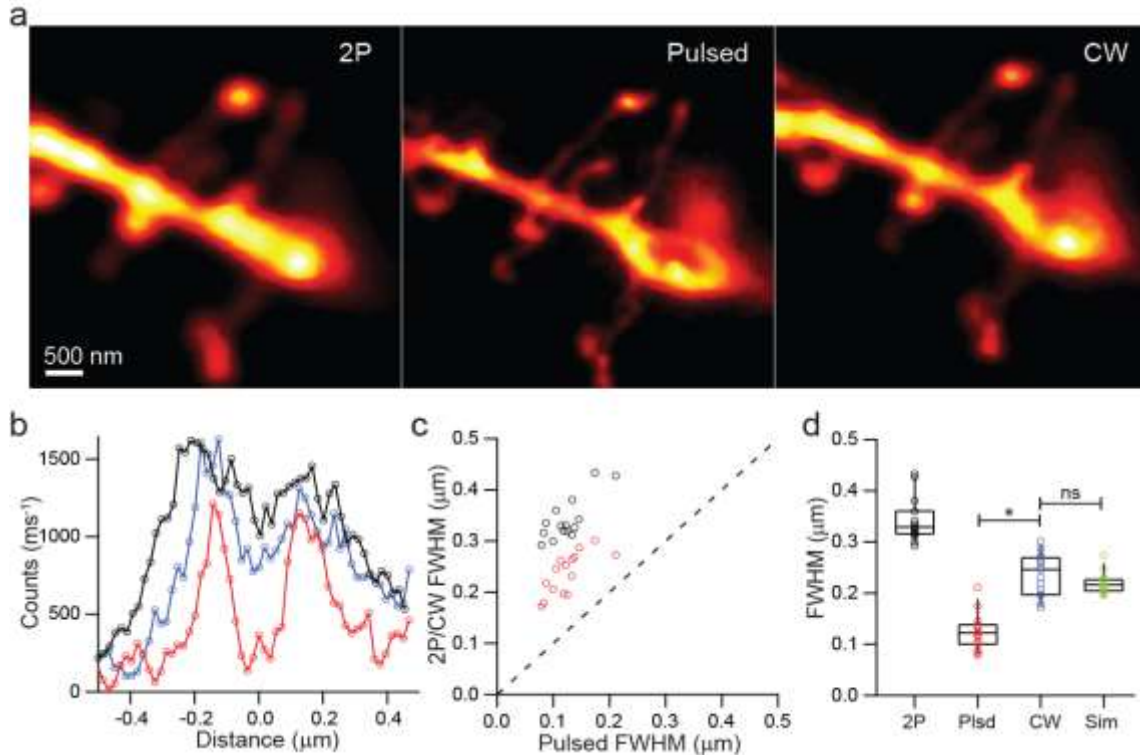


**Figure 4.6 a**, Images of a spiny dendrite taken with 2PLSM (*left*), pulsed STED2P (*middle*), and CW STED2P (*right*). **b**, Line profiles of closely spaced spine necks along the dashed yellow lines in (a) taken by 2PLSM (*black*), CW STED2P (*blue*), and pSTED2P (*red*). Background counts have been subtracted and baselined for display. **c**, Distribution of apparent widths of spine necks ( $n=15$ ) as measured by 2PLSM (*black markers*) and CW STED2P (*red markers*) compared with measurements by pSTED2P. Dashed line indicates unity. **d**, Neck widths measured by 2PLSM (*2P*), pSTED2P (*Plsd*), and CW STED2P (*CW*), and simulated widths (*Sim*) derived from pSTED2P measurements convolved with 170 nm PSF. \*:  $P<0.05$ , ns: not significant (Mann-Whitney rank sum test).

Both modalities showed improvement relative to conventional 2P imaging, and comparison between modes revealed a significant reduction in the apparent spine neck

widths measured by pulsed over CW STED2P (Figure 4.6 b-c). Using the pSTED2P values as the true widths of a model cylindrical neck, we convolved circular cross-sections of the measured neck radii with a Lorentzian PSF of 170 nm width, the resolution predicted by the  $P_{\text{sat}}$  of CW depletion ( $P_{\text{sat}} = 7.2$  mW, Figure 4.3). The resulting distribution of model widths was not statistically different from the distribution of widths measured in CW mode (Figure 4.6 d), suggesting that the improvement in depletion efficiency, as quantified by the smaller  $P_{\text{sat}}$  of pSTED2P, might account for the difference in measurement.

#### **4.3.3. Effect of depth on the resolution of STED imaging in tissue**

Penetration of 2PE imaging in tissue is limited by reduction of signal generation due to scattering and absorption. Similarly, STED resolution enhancement may be impacted by scattering and absorption of depletion light in dense neuropil. To measure the effect of depth on pSTED2P imaging, we imaged dendritic spines at shallow (10-30  $\mu\text{m}$ ) and deep (80-100  $\mu\text{m}$ ) locations in slice (Figure 4.7 a).

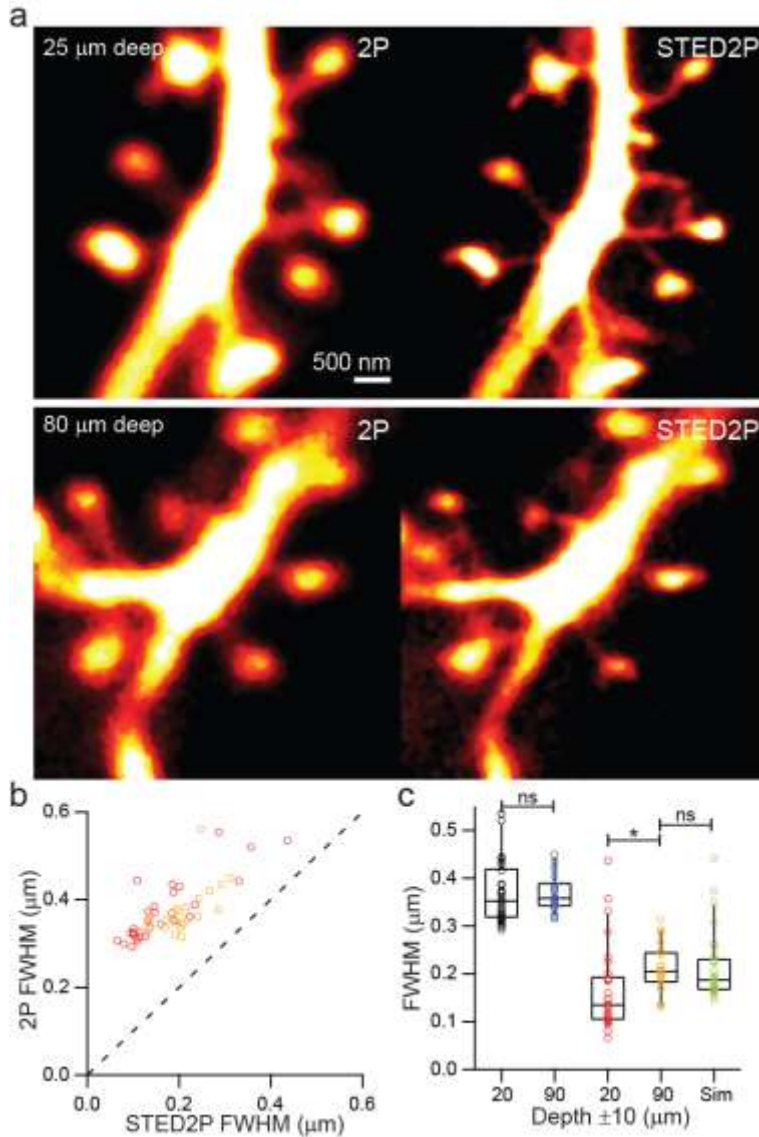


**Figure 4.7 a**, Images of spiny dendrites taken with 2PLSM (*left column*) and pulsed STED2P (*right column*) imaged at 25 μm deep (*top row*) and 80 μm deep (*bottom row*). **b**, Distribution of apparent widths of spine necks as measured by 2PLSM compared with measurements by pSTED2P 10-30 μm deep (n=29, *red markers*) and 80-100 μm deep (n=21, *yellow markers*). Dashed line indicates unity. **c**, Neck widths measured by 2PLSM shallow (*black markers*) and deep (*blue markers*), and by pSTED2P shallow (*red markers*) and deep (*yellow markers*). \*: P<0.05, ns: not significant (Mann-Whitney rank sum test).

pSTED2P images showed reduced neck widths at all depths compared to 2PLSM, and further comparison of the distribution of widths showed clustering around larger values in

the case of deep imaging (Figure 4.7 b). The difference in neck width distributions was statistically significant between the shallow and deep groups ( $p < 0.01$ , Figure 4.7 c). Using the smallest width (132 nm) measured in the deep group as an estimate of the resolution 80-100  $\mu\text{m}$  below the surface of the slice and using the distribution of widths measured in the shallow group as a model distribution for the true spine neck widths, we convolved the shallow distribution of neck widths with a Lorentzian PSF of 132 nm width and found the difference between the model distribution and the deep distribution was not statistically significant (Figure 4.7 c).

#### **4.3.4. Effect of depth on the efficiency of STED**

To examine whether this apparent depth dependence of resolution could reflect depth dependence of depletion efficiency, we removed the helical phase plate and measured the depletion of A594 in dendrites at various depths in the slice (Figure 4.8 a-c).



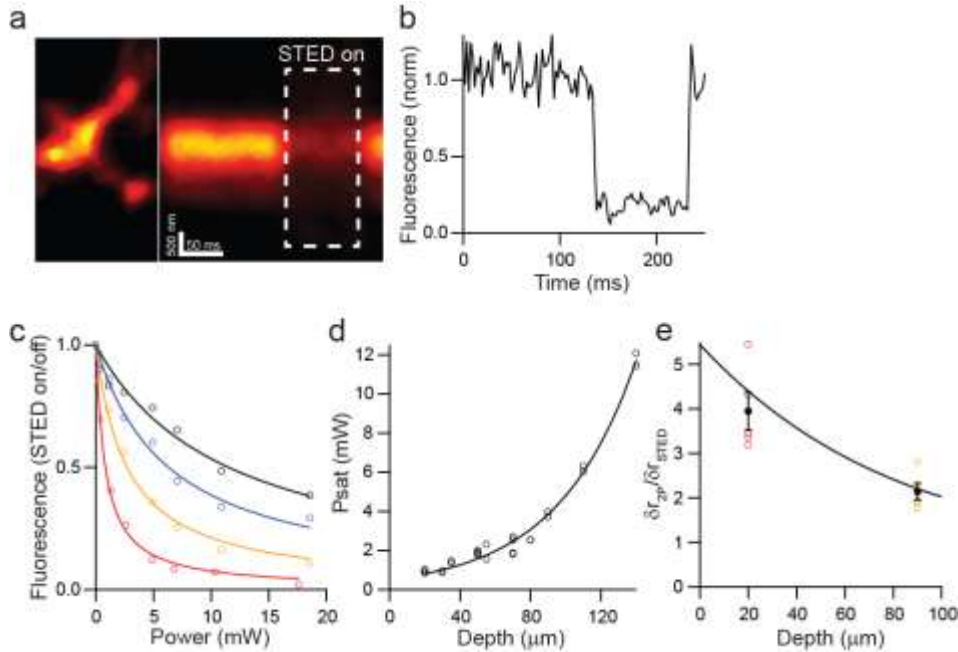


**Figure 4.8 a**, 2PLSM image of spiny dendrite (*left*) and fluorescence collected in linescan mode (*right*) along the dashed line. pSTED light was simultaneously applied during the time period within the white dashed box. The vortex phase plate was withdrawn from the pSTED path to deplete the entire excitation volume. **b**, Fluorescence averaged across the dendrite measured in linescan (a) and normalized to the period before pSTED illumination. **c**, Depletion efficiency versus pSTED laser power measured at 20 (*red*), 70 (*yellow*), 110 (*blue*), and 140 (*black*)  $\mu\text{m}$  deep. Data points were fit to rectangular hyperbolas to determine Psat. **d**, Psat versus depth in slice. Data points were fit to an exponential to determine a surface constant (Psat(0)=0.55 mW) and length constant ( $\lambda=45 \mu\text{m}$ ). **e**, Theoretical improvement in resolution versus depth in slice derived from Eq.1 for 52 mW STED power and modeled with a depth dependent Psat determined from the fit in (d). The width ratio of the 5 smallest necks from Figure 5 shallow (*red markers*) and deep (*yellow markers*) groups are superimposed on the theoretical curve with mean values  $\pm$  SEM (*black markers*).

Psat increased with depth, indicating a decreasing efficiency of depletion (Figure 4.8 d).

The distribution of Psat versus depth was well fit by an exponential of surface constant, Psat(0)=0.55 $\pm$ 0.03 mW, and length constant,  $\lambda=45\pm 2 \mu\text{m}$ . Replacing the constant Isat in Eq.1 with the exponential fit produced a theoretical relation between resolution and depth, indicating resolution enhancement could range from greater than 5-fold close to

the surface to about 2-fold at 100  $\mu\text{m}$  deep (Figure 4.8 e). Comparing the improvement in apparent width of the smallest spine necks in Figure 4.7 with the theoretical resolution curve showed relatively good agreement, with the caveat that improvements in neck width measurements should be smaller on average than the theoretically predicted improvement in resolution due to the finite width of the imaged structures.

Refractive index mismatch between the intended immersion medium of a high numerical aperture objective and the sample results in aberrations that could impede depletion and degrade resolution. While imaging at depths close to 100  $\mu\text{m}$ , we adjusted the correction collar of our microscope objective to examine if the depletion efficiency could be improved (Figure 4.9 a). Depletion should be highly sensitive to aberration of the focus, and Psat increased in general with collar settings different from the “zero” mark defined for use in water (Figure 4.9 b).

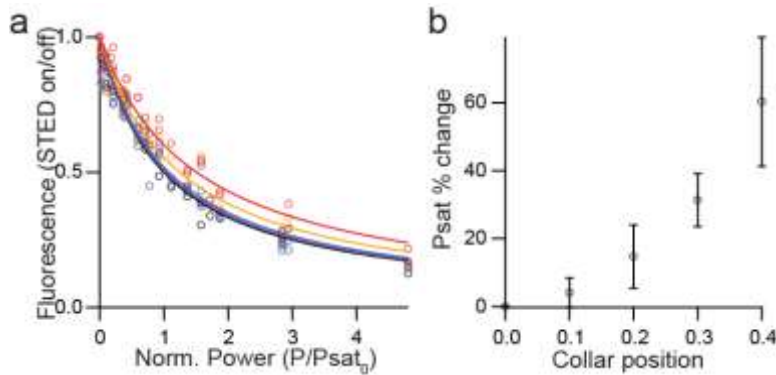


**Figure 4.9 a**, Depletion efficiency of Alexa Fluor-594 in dendrites of neurons close to 100  $\mu\text{m}$  deep in acute brain slices was measured while adjusting the objective correction collar. STED powers were normalized to the Psat measured with the correction collar set to “zero”, Psat<sub>0</sub> (water default), to account for depth dependence in data measured from dendrites at different depths, as in Figure 6. Therefore, differences in the shape of the depletion curves should be attributable to differences resulting from adjusting the correction collar away from its default water setting. Collar settings are 0.0 (*black*), 0.1 (*purple*), 0.2 (*blue*), 0.3 (*yellow*), and 0.4 (*red*). Data points were fitted with rectangular hyperbolas. **b**, Percentage change of Psat resulting from adjustment of the correction collar away from the default water setting (0.0).

As we could not recover the efficiency of depletion power by adjusting the objective's correction collar, this strongly suggests that reduced depletion efficiency at depth is not a result of index mismatch.

#### **4.3.5. Imaging of dendritic spines with 60 nm resolution**

To measure the resolution and image quality achievable with the current design, we imaged a large number of dendritic spines of varying geometries within 30  $\mu\text{m}$  of the tissue surface. Comparison of images obtained with conventional 2PLSM to those acquired with pSTED2P demonstrated enhanced resolution of fine morphological details of spine heads and changes in the apparent sizes of small structures such as spine necks (Figure 4.10 a).

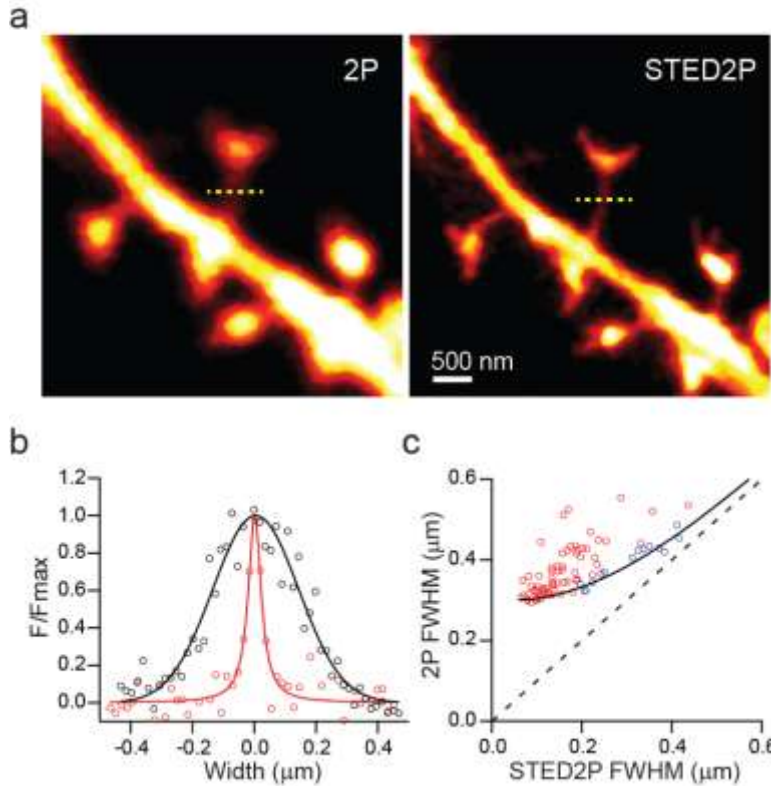


**Figure 4.10 a**, Images of a spiny dendrite taken with 2PLSM (*left*) and pulsed STED 2PLSM (*right*) 16  $\mu\text{m}$  below the tissue surface. Note that spinules emerging from the heads of spines are visualized in the pSTED2P but not in the 2P image. **b**, Line profiles of a thin spine neck along the dashed yellow lines in (a) taken by 2PLSM (*black circles*) and pSTED2P (*red circles*). The data were fitted with a Gaussian of 328 nm FWHM (*black line*) and a Lorentzian of 68 nm FWHM (*red line*). **c**, Distribution of apparent widths of spine necks ( $n=67$ ) as measured by 2PLSM compared with measurements by pSTED2P. The widths of larger, well-isolated features such as spine heads and dendrites were also measured (*blue circles*). Simulated measurements (*black line*) of model data are plotted for 2PLSM and pSTED2P resolutions of 300 nm and 60 nm, respectively. Dashed line indicates unity.

The apparent width of thin necks indicated  $\sim 60$  nm resolution is achievable with our imaging conditions (Figure 4.10 b) without visible signs of photodamage or change in holding current. Measurements of spine necks and heads revealed significant differences in the apparent sizes of structures between 2P and pSTED2P images. Measurements of neck widths in conventional 2P imaging were often contaminated by fluorescence from

the spine head and parent dendrite, resulting in larger differences in measured size than would be expected from the cylindrical geometry of necks alone. Simulation of resolution enhancement for circular structures of varying diameter showed that the apparent width relationship in uncontaminated images is consistent with a 5-fold improvement in imaging resolution (Figure 4.10 c).

#### **4.3.6. Accurate imaging and measurement of dendritic spine morphology**

As an alternative estimate of spine neck dimensions, we inferred the neck radius of isolated spines from the total integrated fluorescence of the neck volume (Figure 4.11 a).

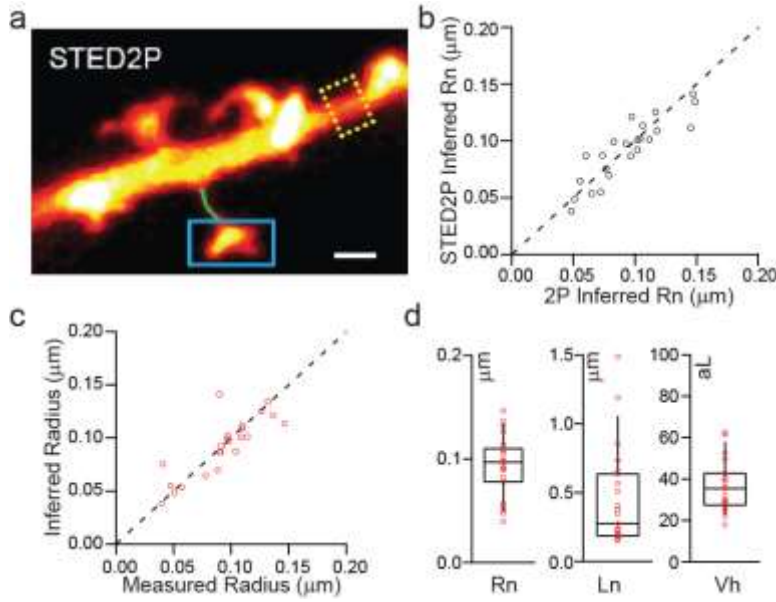


**Figure 4.11 a**, Fluorescence per unit volume was calculated from a smooth portion of dendrite identified in pSTED2P images (*dashed yellow box*) (see text). The width of the dendrite was measured and used to calculate the cylindrical volume. Total fluorescence was integrated over the dendrite in both pSTED2P and 2P images to determine the fluorescence per unit volume for individual images. Total fluorescence from isolated spine necks (*solid green line*) was integrated in both pSTED2P and 2P images and then divided by the fluorescence per unit volume to infer a neck radius in both imaging modes. Spine head volume in pSTED2P images (*solid blue box*) was also calculated in a similar fashion. **b**, Distribution of inferred radii of spine necks imaged by pSTED2P compared with inferred measurements from 2P images, showing the inferred measurement does not depend on imaging resolution. Dashed line indicates unity. **c**, Distribution of spine neck radii inferred from total fluorescence (see text) versus radii measured by pSTED2P. Dashed line indicates unity. **d**, Distributions of spine neck radii (Rn), neck lengths (Ln), and head volumes (Vh) measured by pSTED2P.

Inferred neck radii were calculated from background subtracted STED2P images as follows: a wide, smooth segment of dendrite in each image was selected and modeled as a cylindrical volume of radius  $r_D$  and length  $l_D$ . The width of the dendrite was used to infer the dendritic radius, and the total fluorescence from the segment was integrated and then divided by the calculated volume of the segment to determine the fluorescence per unit volume, denoted here by  $\Gamma_D$ ,

$$\Gamma_D = \frac{\sum f}{\pi r_D^2 l_D} \quad (4.3)$$

$\Gamma_D$  is assumed to depend only on the excitation intensity which varies negligibly over the small field of view ( $5 \mu\text{m} \times 5 \mu\text{m}$ ). The finite z-axis extent of the microscope PSF was also neglected, given the small dimensions of the imaged structures relative to the z-resolution of the microscope ( $\sim 2 \mu\text{m}$  FWHM). The neck volume  $V_N$  was calculated by integrating the neck fluorescence in a rectangular region of interest (ROI) around the neck and dividing by  $\Gamma_D$ . The inferred neck radius  $r_N$  was calculated by modeling the neck as a cylinder and dividing the neck volume by the length of the ROI to determine the cross-sectional area such that

$$r_N = \sqrt{\frac{V_N}{\pi l_N}} \quad (4.4)$$

The boundary of the spine head was identified with a combination of median filtering and thresholding, and the head volume was calculated by dividing the integrated fluorescence within the head by  $\Gamma_D$ . This inferred measurement of the neck radius depends on the conformity of the true neck shape to an ideal cylinder and on the accuracy with which the fluorescence per unit volume can be determined in the large diameter dendrite, and does not depend on the imaging resolution (Figure 4.11 b). Comparison of the inferred widths with the measured widths indicated good agreement (Figure 4.11 c). Agreement between the resolution-independent inferred measurements and resolution-dependent direct measurements indicates spines can be accurately imaged with our microscope parameters up to  $30 \mu\text{m}$  deep. Images of spine necks showed an average diameter of  $0.18 \pm 0.03 \mu\text{m}$  (mean  $\pm$  S.D.), average lengths of  $0.44 \pm 0.35 \mu\text{m}$ , and average head volumes of  $36 \pm 12 \text{ aL}$

(attoliters), in agreement with published results from other high-resolution fluorescence studies and reconstructions by electron microscopy for spines of small size (Arellano et al., 2007; Harris et al., 1992; Izeddin et al., 2011) (Figure 4.11 d).

#### **4.4. Discussion**

I have described the construction and performance of a synchronized, mode-locked STED 2PLSM imaging system, and our results demonstrate the ability of pSTED2P microscopy to achieve resolutions 5-fold beyond the diffraction limit in living tissue. The capability to achieve 60 nm resolution in an acute brain slice under conditions used for electrophysiological analysis allows accurate imaging of dendritic spine morphology and raises the possibility of quantitative studies of the influence of spine geometry on synaptic physiology in brain tissue. For example, computational and theoretical studies examining the effects of spine head and neck shapes on biochemical and electrical compartmentalization could benefit from the combination of superresolution imaging and physiological methods (Holcman and Schuss, 2011). Moreover, the resolution of the pSTED2P microscope and results described here might also be extended to studies of other biological systems where the tissue penetrating capability of 2PLSM has proved useful.

At present, the resolution of pSTED2P at a given depth in turbid tissue appears to be limited mainly by transmission of STED laser light to the focus. Resolution at depth depends on the local intensity of depletion light which will be reduced by propagation through brain tissue due to scattering, absorption, and wavefront deformation (Chaigneau et al., 2011). Forward scatter and absorption losses might be most simply compensated for by increasing the STED laser power as is commonly done in conventional deep tissue



2-photon imaging; however, limitations due to photodamage thresholds and signal-to-background losses may determine the practical ceiling of achievable resolution for a particular fluorophore. Considering the results of this study, perhaps the most promising avenues for further improvement of the achievable depth and resolution will come from advances in fluorescent dye and protein engineering to produce brighter, more photostable, and more efficiently depletable fluorophores better suited for STED imaging (Morozova et al., 2010), as well as from novel methods to correct for instrument and sample-induced deformations of the STED focus (Ji et al., 2010).

## **5. Application of pSTED2P to studying the biophysics of dendritic spines**

### **5.1.Introduction**

Dendritic spines are located on the dendrites of many principal classes of neurons of the cortex, hippocampus, striatum, and cerebellum. These structures, characterized by a “head” containing a postsynaptic density (PSD) attached to its parent dendrite by a “neck,” are responsible for receiving the majority of excitatory synaptic transmission in the mammalian brain. The synapses of spines display both biochemical and electrical activity in response to stimulation (Bloodgood and Sabatini, 2007; Harvey et al., 2008; Lee et al., 2009), and spiny synapses have been shown to support many forms of structural and functional plasticity (Harvey et al., 2008; Kwon and Sabatini, 2011; Matsuzaki et al., 2004; Yasuda et al., 2003). Despite the abundance of insight into synaptic physiology, questions persist regarding the correspondence between the structure of spines and their biochemical and electrical functions (Nimchinsky et al., 2002).

### **5.2.Dendritic spines as biochemical compartments**

#### **5.2.1. Diffusive compartmentalization in dendritic spines**

The morphology of dendritic spines imposes geometric constraints on the diffusion of biochemical materials within the spine and between the spine and its parent dendrite. A simple model describing transfer of freely diffusing substances between the spine head and dendrite can be obtained by approximating the spine head and dendrite as compartments of homogeneous concentration separated by a passive barrier imposed by the spine neck (Svoboda et al., 1996). The only time varying quantity in this model is the concentration in the spine head,  $C_H(t)$ , while constant parameters are the cytoplasmic diffusion coefficient,  $D$ , the volume of the spine head,  $V_H$ , the concentration in the

dendrite,  $C_d$ , which functions as a particle reservoir and can be set to 0, and the geometric resistance of the spine neck,  $W_N$ , which relates the dimensions of the neck to a resistance to diffusive transfer across it. The equation governing the time course of  $C_H$  is then

$$\frac{dC_H}{dt} = -\frac{D}{V_H W_N} C_H \quad (5.1)$$

This behavior is directly analogous to capacitive discharge in an electrical RC circuit, and there is an analogous correspondence of the geometry of a resistor and its resistance to the diffusive resistance of the spine neck. That is,

$$W_N = \frac{l_N}{a_N} \quad (5.2)$$

where  $l_N$  is the neck length, and  $a_N$  is its cross-sectional area. Given a step change in concentration, (5.1) and (5.2) predict exponential relaxation with a recovery time given by

$$\tau = \frac{V_H l_N}{D a_N}. \quad (5.3)$$

Experiments performed by various groups have investigated correlations between diffusive transfer of calcium, small molecules, and proteins with neck morphological parameters, and modulation of diffusive transfer in response to perturbations. Notably, activity dependent plasticity of diffusive transfer of both small molecules and proteins has been observed (Bloodgood and Sabatini, 2005), and the differences in diffusive state could not be accounted for by considering spine head volume and neck length according to (5.3), thus highlighting the possible involvement of activity induced remodeling of spine neck width. However, experiments performed with conventional fluorescence

microscopy have been unable to measure sub-resolution features, such as the diameters of many spine necks, and thus have not been able to fully address the role of spine neck morphology in diffusive transfer. Indeed, studies have used diffusive measurements, such as tracking calcium spread (Noguchi et al., 2005) or fluorescence recovery after photobleaching (Grunditz et al., 2008), as functional measurements of spine neck geometry to circumvent the absence of methods to measure neck width directly. At the same time, recent theoretical work has clarified the approximations and limits of the simple model underlying (5.3) (Holcman and Schuss, 2011). Thus, there are theoretical, as well as biological, reasons to question the broad validity of (5.3), and the examination of diffusive transfer with accurate measurement of morphology is necessary to better understand how morphological plasticity and heterogeneity might influence the biochemical function of dendritic spines.

### **5.2.2. Morphological determinants of diffusional transfer in dendritic spines**

In order to observe diffusional transfer across the spine neck, we performed fluorescence recovery after photobleaching (FRAP) to measure the relaxation of a step perturbation to concentration of fluorescent dye in the spine head. Spine heads were visualized under pSTED2P for morphological analysis (Figure 5.1 a), and fluorescence from the spine head was measured over time by line scanning with conventional 2PLSM (Figure 5.1 b).

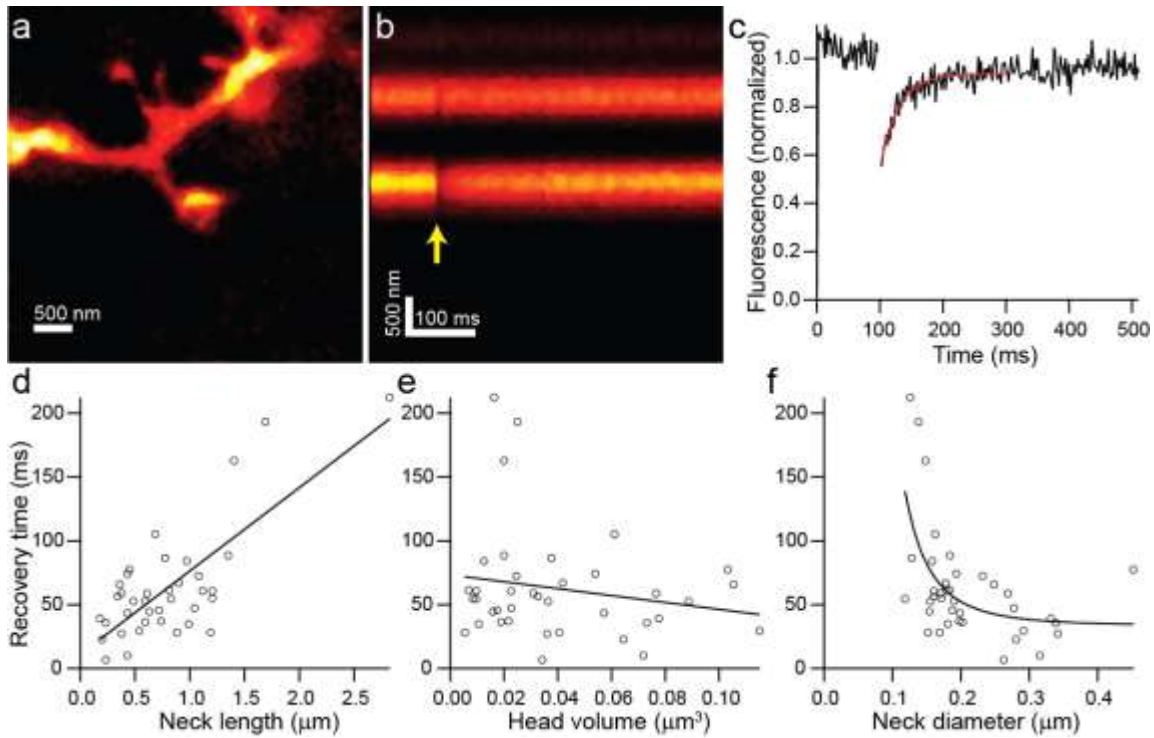


**Figure 5.1** **a**, pSTED2P image of a dendritic spine. **b**, 2PLSM linescan taken through the spine and dendrite in (a). The 0.5 ms photobleaching pulse was delivered on the spine head after a 100 ms delay (*yellow arrow*). **c**, Fluorescence in the spine head over time quantified from (b). Recovery was fit with a decaying exponential (*red line*) to obtain the recovery time constant. **d**, Recovery time constants plotted against neck length; **e**, against head volume; **f**, and against neck diameter.

During the line scan, the spine head was exposed to 0.5 ms illumination with ~100 fs laser pulses centered on 720 nm from a third mode-locked Ti:sapphire laser (Chameleon XR), producing a rapid reduction in head fluorescence attributable to photobleaching, followed by a recovery period driven by diffusional transfer across the neck (Figure 5.1 c).

To identify morphological determinants of diffusional transfer, we compared FRAP recovery times against morphological measurements obtained with pSTED2P. Recovery times showed strong linear correlation with neck length ( $r=0.75$ ,  $p<0.0001$ ,  $n=38$ ) (Figure 5.1 d), but no significant correlation with head volume ( $r=-0.19$ ,  $p=0.26$ ,

n=38). The dependence of recovery time on neck diameter appeared nonlinear and was fit by a power function,  $f(x) = a + bx^n$ , with  $n = -3.28 \pm 1.79$ . These findings demonstrate that the dependence of diffusive transfer on morphological parameters and on the neck diameter in particular can be addressed with pSTED2P.

To examine the validity of the simple model leading to (5.3), we compared recovery times against a parameter defined as a combination of morphological

parameters,  $\zeta \equiv \frac{V_H l_N}{d_N^2}$ , so that (5.3) becomes

$$\tau = \frac{4}{\pi D} \zeta . \quad (5.4)$$

Comparison of recovery time against  $\zeta$  showed strong linear correlation ( $r=0.76$ ,  $p < 0.0001$ ,  $n=38$ ) and was well fit by a line with a slope of  $44 \pm 7$  (Figure 5.2 a).

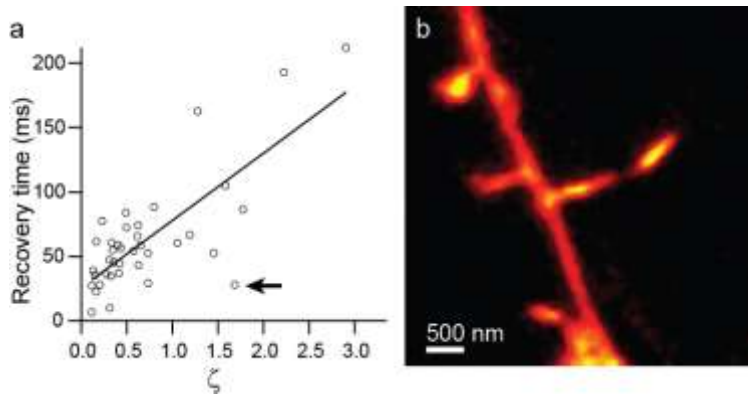


**Figure 5.2 a**, Recovery times from **Figure 5.1** plotted against  $\zeta$  . **b**, pSTED2P image of the spine producing the outlying point marked by the arrow in (a).

Given (5.4), this slope value yields an estimate for the diffusion coefficient,  $D = 29 \mu\text{m}^2/\text{s}$ , which is nearly 10-fold smaller than a value taken from the literature for free intracellular diffusion measured in *Xenopus* oocytes (Nitsche et al., 2004). This discrepancy may be the result of differences in methodology (FRAP vs. dye spreading) or may reflect actual

differences in the local cytoplasmic environment. In support of the latter possibility, measurement of the diffusion coefficients of small molecule fluorophores in the dendrites of stellate cells has also shown a near 10-fold slowing, perhaps attributable to special properties of the dendroplasm (Soler-Llavina and Sabatini, 2006). Another possibility is that the model justifying (5.4) is not entirely valid in these conditions. It may be that outliers exhibit unusual morphologies that violate the assumptions underlying (5.3), as in the case of the spine shown in (Figure 5.2 b) in which the head size and width is similar to that of the neck.

### **5.3.Dendritic spines as electrical compartments**

#### **5.3.1. Electrical compartmentalization in dendritic spines**

The possibility of morphology regulating electrical activity in dendritic spines has long been a controversial topic (Tsay and Yuste, 2004). Numerous experimental studies have addressed whether the passive geometry of spines has a measurable impact on electrical signaling through affecting the generation and propagation of membrane potentials during synaptic transmission, and the results of these studies have provided evidence supporting (Bloodgood and Sabatini, 2005; Bloodgood et al., 2009; Harnett et al., 2012) and rejecting (Koch and Zador, 1993; Palmer and Stuart, 2009; Svoboda et al., 1996) the role of spine geometry in regulating electrical function of spines. One immediate difficulty of determining the electrical role of spine morphology is that direct measurement of spine morphology, particularly the dimensions of the spine neck, has not been possible with conventional fluorescence imaging. Thus, the ability to accurately measure spine morphology conferred by pSTED2P could be of great benefit to further progress in this area.

### **5.3.2. Morphological determinants of electrical compartmentalization of spines**

Measurement of the subthreshold membrane potential within a dendritic spine is technically challenging due to poor electrophysiological access and the lack of optical voltage indicators with sufficient sensitivity to measure small depolarizations. Calcium influx through endogenous voltage-dependent sources, such as voltage-sensitive calcium channels (VSCC's) and the NMDA-type glutamate receptor (NMDAR), can be used as a substitute for direct measurement of spine voltage, as calcium indicators are readily available with sensitivity and speed sufficient to report calcium transients due to subthreshold stimuli. As a first step toward exploring the relationship between spine morphology and electrical compartmentalization, we combined two-photon photolysis of caged glutamate (Matsuzaki et al., 2001), whole-cell electrophysiology, and calcium imaging, with pSTED2P for morphological imaging.

Hippocampal acute slices were prepared and CA1 pyramidal neurons were whole-cell patch clamped at near-physiological temperature (34° C), as described in the previous chapter. 3 mM methoxy-nitroindoliny-caged glutamate (MNI-glutamate) was added to the ACSF with 10  $\mu$ M D-serine to prevent glutamate receptor desensitization. Whole-cell patch pipettes were filled with a KMeSO<sub>4</sub>-based internal solution containing 300  $\mu$ M Alexa Fluor 594 and 300  $\mu$ M Fluo-5F, a moderate affinity calcium indicator (Kd ~2  $\mu$ M). Cells were allowed to dye fill for 15-20 minutes after break-in before beginning the experiment.

Dendritic spines were visualized by 2PLSM and pSTED2P (Figure 5.3 a).



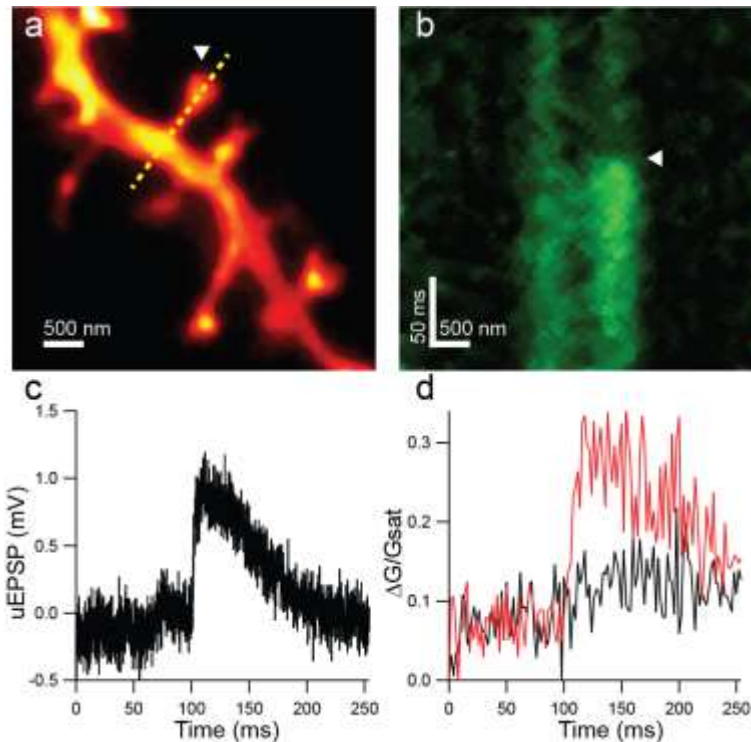


**Figure 5.3** **a**, pSTED2P image of dendritic spines. MNI-glutamate was uncaged at a point located near a target spine (*white arrowhead*) while line scanning over the spine and dendrite (*yellow dashed line*). **b**, Green fluorescence measured in line scan. MNI-glutamate uncaging following a 100 ms delay (*white arrowhead*) produced a transient increase in green fluorescence. **c**, Somatic membrane potential recording the uEPSP elicited from the synapse in (a). **d**, Quantification of Fluo-5F fluorescence in the spine head (*red*) and in the dendrite (*black*) as imaged in (b).

No shifts in holding current or increase in green fluorescence was observed during pSTED2P imaging, likely due to the relatively low two-photon cross-section of MNI-glutamate (0.06 GM) contributing to poor excitation by the dispersed STED pulse. Before uncaging, the system was switched into current clamp with current injection to maintain a resting potential near -60 mV. While line scanning over the dendrite and spine, delivery of 0.5 ms illumination with ~100 fs laser pulses centered on 720 nm from a third mode-locked Ti:sapphire laser (Chameleon XR) generated transient increases in green fluorescence selectively in the spine head, as well as small depolarizations measured at

the soma (Figure 5.3 b-d). Green fluorescence from calcium-bound Fluo-5F was first normalized to red fluorescence from Alexa594 (G/R) to account for volume variation of the intracellular space, and then normalized again to the saturated G/R ratio ((G/R)sat) corresponding to the fully bound indicator as described in (Bloodgood and Sabatini, 2007) to obtain a measurement of calcium influx (G/Gsat) comparable across microscopes with varying collection efficiencies.

To investigate potential correlations between the amplitude of uncaging-evoked excitatory postsynaptic potentials (uEPSP's) and peak changes in green fluorescence ( $\Delta G/G_{sat}$ ) with spine morphology, we compared these measurements against measurements of spine neck diameter and length (Figure 5.4).

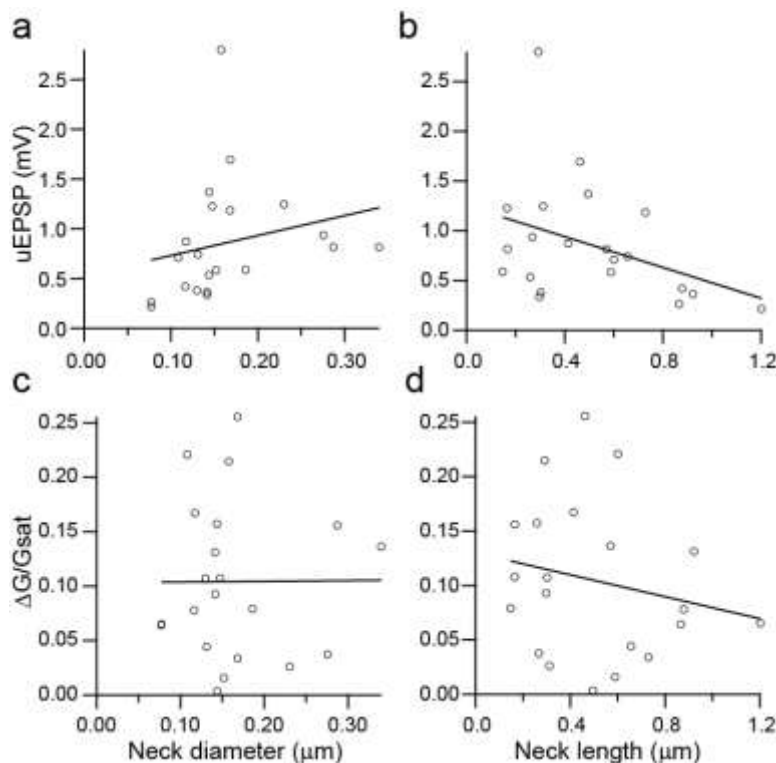


**Figure 5.4** **a**, uEPSP amplitude plotted against spine neck diameter and **b**, against neck length. **c**, Amplitude of calcium transient plotted against neck diameter and **d**, neck length.

No significant correlations were observed between uEPSP amplitude and neck diameter ( $r=0.23$ ,  $p=0.32$ ,  $n=21$ ; Figure 5.4 a), peak calcium and neck diameter ( $r=0.23$ ,  $p=0.98$ ,  $n=21$ ; Figure 5.4 c), or peak calcium and neck length ( $r=-0.20$ ,  $p=0.38$ ,  $n=21$ ; Figure 5.4 d). A weak negative correlation was observed between uEPSP amplitude and neck length ( $r=-0.38$ ,  $p=0.09$ ,  $n=21$ ; Figure 5.4 b).

#### **5.4.Discussion**

I have described the application of pSTED2P to biophysical studies relating diffusion and electrical compartmentalization with spine morphology. Morphological determinants of fluorescence recovery time were identified and evaluated within the context of a simple compartmental model describing diffusive transfer between spine and dendrite.

Correlations in uEPSP's and calcium transients with neck geometry were also investigated. However, the large variability present in the uEPSP and calcium measurements will likely require large  $N$  to be tractable by correlative approaches.

Nevertheless, we have demonstrated the usefulness of pSTED2P in combination with other optical and electrophysiological techniques to the study of dendritic spine biophysics.

## **6. Summary and future directions**

### **6.1. Thesis summary**

The aim of the work described in this thesis was to develop a method of superresolution fluorescence microscopy applicable to imaging neurons in thick samples of living tissue and then demonstrate applications of this method for neurobiological studies. To fulfill this aim, we achieved the following:

- Designed and constructed a two-photon microscope combined with STED to achieve superresolution fluorescence imaging in acute brain slices
- Experimentally characterized effects of pulsing and polarization on suppression of two-photon excited fluorescence
- Experimentally compared performance of CW and pulsed STED for superresolution imaging in tissue
- Experimentally characterized the effect of imaging depth in tissue on resolution and depletion efficiency
- Examined the relationship of spine morphology and neck diameter with diffusive transfer
- Examined the relationship of spine neck morphology with the postsynaptic response to glutamate photorelease

### **6.2. Future directions**

#### **6.2.1. Improving depth penetration of two-photon excitation STED microscopy**

The loss of resolution limiting the depth penetration of STED2P is an important technical hurdle toward the general application of this technique. The results of Chapter 4 suggest that the loss of resolution might be explained by the effect of laser propagation in tissue on the STED process itself, reflected in the exponential decay of depletion efficiency

with depth. Furthermore, this decay did not appear to be the result of aberrations due to refractive index mismatching in the tissue, as better depletion could not be recovered by the use of the objective correction collar. Additional work is needed to understand the mechanisms contributing to the measured length constant, which might provide further inspiration for methods of improving penetration.

Methods of improving focusing in tissue have been demonstrated through spatial and temporal manipulation of laser light. The use of phase-patterning instruments, such as spatial light modulators and deformable mirrors, has enabled techniques such as adaptive wavefront engineering (Ji et al., 2010) and phase conjugation (Yaqoob et al., 2008) to correct for propagation through tissue. Additional work exploring the use of these techniques for improving depth penetration of STED is likewise needed.

### **6.2.2. Identification and implementation of alternative fluorophores**

The live cell imaging described in this thesis was performed with Alexa Fluor 594 as our fluorophore of choice. Alexa594 is a water soluble, non-toxic dye with relatively high brightness and photostability as compared with other organic dyes, and is frequently included in whole-cell internal solutions to be loaded into neurons by patch pipette for space filling and electrophysiology in combination with two-photon imaging. Common availability and ease of use make Alexa594 an advantageous option for use in STED2P, but testing of alternative fluorophores (Morozova et al., 2010) may yield exciting opportunities.

Of particular interest for STED-type superresolution are reversibly switchable fluorescent proteins (RSFP's) shown to be advantageous due to the high efficiency of

photoswitching generally requiring orders of magnitude less intensity than STED (Testa et al., 2012).

### **6.2.3. Biophysical, structural, and functional studies of nanoscale systems**

The experiments described in chapter 5 demonstrate the use of pSTED2P for structure-function studies in combination with experimental methods such as FRAP, whole-cell electrophysiology, caged neurotransmitter photolysis, and calcium imaging. These studies could be extended to new experimental conditions or other biological systems in which nanoscale structure is of interest. For example, similar studies could be performed on dendritic spines of other cell types, such as spiny projection neurons of the striatum or Purkinje cells of the cerebellum, or on spines with perturbed structure and function in models of disease, such as tuberous sclerosis complex (Tavazoie et al., 2005) or Alzheimer's disease (Shankar et al., 2008).

Alternatively, biophysical studies of dendritic spines could be improved upon with the application of novel techniques. For example, the study of electrical compartmentalization and the role of spine geometry in regulating electrical signaling would benefit from methods able to directly measure membrane potential by an optical signal (Jin et al., 2012; Kralj et al., 2011).

## Reference List

- A. J. Bain, R. J. Marsh, D. A. Armoogum, O. Mongin, L. PorrÃ³s, and M. Blanchard-desce. (2008). Time-resolved stimulated emission depletion in two-photon excited states.
- Abbe, E. (1873). BeitrÃ¤ge zur Theorie des Mikroskops und der mikroskopischen Wahrnehmung. *Archiv FÃ¼r Mikroskopische Anatomie* 9, 413-418.
- Arellano, J.I., Benavides-Piccione, R., Defelipe, J., and Yuste, R. (2007). Ultrastructure of dendritic spines: correlation between synaptic and spine morphologies *Front. Neurosci.* 1, 131-143.
- Bertero, M., and Boccacci, P. *Introduction to inverse problems in imaging*. Oxford: Taylor & Francis, 1998. Print.
- Betzig, E., Patterson, G.H., Sougrat, R., Lindwasser, O.W., Olenych, S., Bonifacino, J.S., Davidson, M.W., Lippincott-Schwartz, J., and Hess, H.F. (2006). Imaging intracellular fluorescent proteins at nanometer resolution *Science* 313, 1642-1645.
- Bloodgood, B.L., Giessel, A.J., and Sabatini, B.L. (2009). Biphasic synaptic Ca influx arising from compartmentalized electrical signals in dendritic spines *PLoS Biol.* 7, e1000190.
- Bloodgood, B.L., and Sabatini, B.L. (2007). Nonlinear regulation of unitary synaptic signals by CaV(2.3) voltage-sensitive calcium channels located in dendritic spines *Neuron* 53, 249-260.
- Bloodgood, B.L., and Sabatini, B.L. (2005). Neuronal activity regulates diffusion across the neck of dendritic spines *Science* 310, 866-869.
- Chaigneau, E., Wright, A.J., Poland, S.P., Girkin, J.M., and Silver, R.A. (2011). Impact of wavefront distortion and scattering on 2-photon microscopy in mammalian brain tissue *Opt. Express* 19, 22755-22774.
- Deng, S., Liu, L., Cheng, Y., Li, R., and Xu, Z. (2010). Effects of primary aberrations on the fluorescence depletion patterns of STED microscopy. *Optics Express* 18, 1657-1666.
- Denk, W., Strickler, J.H., and Webb, W.W. (1990). Two-photon laser scanning fluorescence microscopy. *Science* 248, 73-76.
- Ding, J.B., Takasaki, K.T., and Sabatini, B.L. (2009). Supraresolution imaging in brain slices using stimulated-emission depletion two-photon laser scanning microscopy *Neuron* 63, 429-437.

Grunditz, A., Holbro, N., Tian, L., Zuo, Y., and Oertner, T.G. (2008). Spine neck plasticity controls postsynaptic calcium signals through electrical compartmentalization *J. Neurosci.* 28, 13457-13466.

Gustafsson, M.G. (2005). Nonlinear structured-illumination microscopy: wide-field fluorescence imaging with theoretically unlimited resolution *Proc. Natl. Acad. Sci. U. S. A.* 102, 13081-13086.

Harke, B., Keller, J., Ullal, C.K., Westphal, V., Schonle, A., and Hell, S.W. (2008). Resolution scaling in STED microscopy *Opt. Express* 16, 4154-4162.

Harnett, M.T., Makara, J.K., Spruston, N., Kath, W.L., and Magee, J.C. (2012). Synaptic amplification by dendritic spines enhances input cooperativity *Nature* 491, 599-602.

Harris, K.M., Jensen, F.E., and Tsao, B. (1992). Three-dimensional structure of dendritic spines and synapses in rat hippocampus (CA1) at postnatal day 15 and adult ages: implications for the maturation of synaptic physiology and long-term potentiation *J. Neurosci.* 12, 2685-2705.

Harvey, C.D., Yasuda, R., Zhong, H., and Svoboda, K. (2008). The spread of Ras activity triggered by activation of a single dendritic spine *Science* 321, 136-140.

Holcman, D., and Schuss, Z. (2011). Diffusion laws in dendritic spines *J. Math. Neurosci.* 1, 10.

Iketaki, Y., Watanabe, T., Bokor, N., and Fujii, M. (2007). Investigation of the center intensity of first- and second-order Laguerre-Gaussian beams with linear and circular polarization. *Opt. Lett.* 32, 2357-2359.

Izeddin, I., Specht, C.G., Lelek, M., Darzacq, X., Triller, A., Zimmer, C., and Dahan, M. (2011). Super-resolution dynamic imaging of dendritic spines using a low-affinity photoconvertible actin probe *PLoS One* 6, e15611.

Ji, N., Milkie, D.E., and Betzig, E. (2010). Adaptive optics via pupil segmentation for high-resolution imaging in biological tissues *Nat. Methods* 7, 141-147.

Jin, L., Han, Z., Platasa, J., Woollorton, J.R., Cohen, L.B., and Pieribone, V.A. (2012). Single action potentials and subthreshold electrical events imaged in neurons with a fluorescent protein voltage probe. *Neuron* 75, 779-785.

Keller, J., Schonle, A., and Hell, S.W. (2007). Efficient fluorescence inhibition patterns for RESOLFT microscopy *Opt. Express* 15, 3361-3371.

Klar, T.A., Jakobs, S., Dyba, M., Egner, A., and Hell, S.W. (2000). Fluorescence microscopy with diffraction resolution barrier broken by stimulated emission *Proc. Natl. Acad. Sci. U. S. A.* 97, 8206-8210.



- Koch, C., and Zador, A. (1993). The function of dendritic spines: devices subserving biochemical rather than electrical compartmentalization *J. Neurosci.* *13*, 413-422.
- Kralj, J.M., Douglass, A.D., Hochbaum, D.R., Maclaurin, D., and Cohen, A.E. (2011). Optical recording of action potentials in mammalian neurons using a microbial rhodopsin. *Nature Methods* *9*, 90-95.
- Kwon, H.B., and Sabatini, B.L. (2011). Glutamate induces de novo growth of functional spines in developing cortex *Nature* *474*, 100-104.
- Lee, S.J., Escobedo-Lozoya, Y., Szatmari, E.M., and Yasuda, R. (2009). Activation of CaMKII in single dendritic spines during long-term potentiation *Nature* *458*, 299-304.
- Leutenegger, M., Eggeling, C., and Hell, S.W. (2010). Analytical description of STED microscopy performance *Opt. Express* *18*, 26417-26429.
- Matsuzaki, M., Ellis-Davies, G.C., Nemoto, T., Miyashita, Y., Iino, M., and Kasai, H. (2001). Dendritic spine geometry is critical for AMPA receptor expression in hippocampal CA1 pyramidal neurons. *Nat. Neurosci.* *4*, 1086-1092.
- Matsuzaki, M., Honkura, N., Ellis-Davies, G.C., and Kasai, H. (2004). Structural basis of long-term potentiation in single dendritic spines *Nature* *429*, 761-766.
- Mertz, J. *Introduction to optical microscopy*. Colorado: Roberts and Co, 2010. Print.
- Moneron, G., and Hell, S.W. (2009). Two-photon excitation STED microscopy. *Opt. Express* *17*, 14567-14573.
- Morozova, K.S., Piatkevich, K.D., Gould, T.J., Zhang, J., Bewersdorf, J., and Verkhusha, V.V. (2010). Far-red fluorescent protein excitable with red lasers for flow cytometry and superresolution STED nanoscopy *Biophys. J.* *99*, L13-5.
- Nimchinsky, E.A., Sabatini, B.L., and Svoboda, K. (2002). Structure and function of dendritic spines *Annu. Rev. Physiol.* *64*, 313-353.
- Nitsche, J.M., Chang, H., Weber, P.A., and Nicholson, B.J. (2004). A Transient Diffusion Model Yields Unitary Gap Junctional Permeabilities from Images of Cell-to-Cell Fluorescent Dye Transfer Between *Xenopus* Oocytes. *Biophys. J.* *86*, 2058-2077.
- Noguchi, J., Matsuzaki, M., Ellis-Davies, G.C., and Kasai, H. (2005). Spine-neck geometry determines NMDA receptor-dependent Ca<sup>2+</sup> signaling in dendrites *Neuron* *46*, 609-622.
- Palmer, L.M., and Stuart, G.J. (2009). Membrane potential changes in dendritic spines during action potentials and synaptic input *J. Neurosci.* *29*, 6897-6903.

- Pologruto, T.A., Sabatini, B.L., and Svoboda, K. (2003). ScanImage: flexible software for operating laser scanning microscopes *Biomed. Eng. Online* 2, 13.
- Richards, B., and Wolf, E. (1959). Electromagnetic diffraction in optical systems. II. Structure of the image field in an aplanatic system. *Proceedings of the Royal Society of London. Series A. Mathematical and Physical Sciences* 253, 358-379.
- Rust, M.J., Bates, M., and Zhuang, X. (2006). Sub-diffraction-limit imaging by stochastic optical reconstruction microscopy (STORM) *Nat. Methods* 3, 793-795.
- Shankar, G.M., Li, S., Mehta, T.H., Garcia-Munoz, A., Shepardson, N.E., Smith, I., Brett, F.M., Farrell, M.A., Rowan, M.J., Lemere, C.A., *et al.* (2008). Amyloid-beta protein dimers isolated directly from Alzheimer's brains impair synaptic plasticity and memory *Nat. Med.* 14, 837-842.
- Soler-Llavina, G.J., and Sabatini, B.L. (2006). Synapse-specific plasticity and compartmentalized signaling in cerebellar stellate cells *Nat. Neurosci.* 9, 798-806.
- Svoboda, K., Tank, D.W., and Denk, W. (1996). Direct measurement of coupling between dendritic spines and shafts *Science* 272, 716-719.
- Takasaki, K.T., Ding, J.B., and Sabatini, B.L. (2013). Live-cell superresolution imaging by pulsed STED two-photon excitation microscopy. *Biophys. J.* 104, 770-777.
- Tavazoie, S.F., Alvarez, V.A., Ridenour, D.A., Kwiatkowski, D.J., and Sabatini, B.L. (2005). Regulation of neuronal morphology and function by the tumor suppressors Tsc1 and Tsc2 *Nat. Neurosci.* 8, 1727-1734.
- Testa, I., Urban, N.T., Jakobs, S., Eggeling, C., Willig, K.I., and Hell, S.W. (2012). Nanoscopy of living brain slices with low light levels. *Neuron* 75, 992-1000.
- Tsay, D., and Yuste, R. (2004). On the electrical function of dendritic spines *Trends Neurosci.* 27, 77-83.
- Willig, K.I., Harke, B., Medda, R., and Hell, S.W. (2007). STED microscopy with continuous wave beams. *Nat. Methods* 4, 915-918.
- Yan, Y., Hoffmann, H., Makarsky, A., Richter, W., and Talmon, Y. (2007). Swelling of  $L\alpha$ -Phases by Matching the Refractive Index of the Water-Glycerol Mixed Solvent and that of the Bilayers in the Block Copolymer System of (EO) 15-(PDMS) 15-(EO) 15. *The Journal of Physical Chemistry B* 111, 6374-6382.
- Yaqoob, Z., Psaltis, D., Feld, M.S., and Yang, C. (2008). Optical phase conjugation for turbidity suppression in biological samples. *Nature Photonics* 2, 110-115.

Yasuda, R., Sabatini, B.L., and Svoboda, K. (2003). Plasticity of calcium channels in dendritic spines *Nat. Neurosci.* 6, 948-955.